MODELING THE NUCLEAR INFRARED SPECTRAL ENERGY DISTRIBUTION
OF TYPE II ACTIVE GALACTIC NUCLEI

Paulina Lira[1], Liza Videla[1], Yanling Wu[2], Almudena Alonso-Herrero[3], David M. Alexander[4], and Martin Ward[4]

[1] Departamento de Astronomía, Universidad de Chile, Santiago, Chile
[2] Infrared Processing and Analysis Center, California Institute of Technology, Pasadena, CA, USA
[3] Instituto de Física de Catabria, CSIC-UC, E-39005 Santander, Spain
[4] Department of Physics, Durham University, South Road, Durham DH1 3LE, UK

ABSTRACT

We present results from model fitting to the spectral energy distribution (SED) of a homogeneous sample of Seyfert II galaxies drawn from the $12\,\mu$m Galaxy Sample. Imaging and nuclear flux measurements are presented in an accompanying paper. Here we add *Spitzer*/IRS observations to further constrain the SEDs after careful subtraction of a starburst component. We use the library of CLUMPY torus models from Nenkova et al. and also test the two-phase models recently produced by Stalevski et al. We find that photometric and spectroscopic observations in the mid-IR ($\lambda \gtrsim 5\,\mu$m) are crucial to properly constrain the best-fit torus models. About half of our sources show clear near-IR excess of their SEDs above the best-fit models. This problem can be less severe when using the Stalevski et al. models. The nature of this emission is not clear since best-fitted blackbody temperatures are very high ($\sim$1700–2500 K) and the Type II classification of our sources would correspond to a small probability to peer directly into the hottest regions of the torus. Crucially, the derived torus parameters are quite robust when using CLUMPY models, independently of whether or not the sources require an additional blackbody component. Our findings suggest that tori are characterized by $\mathcal{N}_0 \gtrsim 5$, $\sigma \gtrsim 40$, $\tau \lesssim 25$, $\angle i \gtrsim 40°$, $Y \lesssim 50$, and $A_v^{\mathrm{los}} \sim 100$–300, where $\mathcal{N}_0$ is the number of clouds in the equatorial plane of the torus, σ is the characteristic opening angle of the cloud distribution, τ is the opacity of a single cloud, $\angle i$ is the line-of-sight orientation of the torus, Y is the ratio of the inner to the outer radii, and A_v^{los} is the total opacity along the line of sight. From these, we can determine typical torus sizes and masses of 0.1–5.0 pc and 10^4–$10^6\,M_\odot$, respectively. We find tentative evidence that those nuclei with detected hidden broad-line regions are characterized by lower levels of extinction than those without one. Finally, we find no correlation between the torus properties and the presence of circumnuclear or more global star formation.

Key word: galaxies: Seyfert

Online-only material: color figures

1. INTRODUCTION

Evidence for the presence of circumnuclear obscuration in active galactic nuclei (AGNs) is undeniable. Obscuration has been determined from the excess absorption in X-ray, UV, and optical wavelengths (Lawrence & Elvis 1982; Mass-Hesse et al. 1993; Turner et al. 1997; Malkan et al. 1998; Risaliti et al. 1999; see also references in Videla et al. 2013, hereafter Paper I). However, whether this obscuration has similar properties in all sources or presents a wide variety of properties that vary from source to source is not yet determined.

From a statistical viewpoint, there is strong evidence that the properties of the obscuring material change as a function of luminosity, and possibly, redshift (Barger et al. 2005; Hopkins et al. 2007; Gilli et al. 2007). Still, because of the higher spatial resolution, only local intermediate-luminosity ($\lesssim 10^{46}$ erg s^{-1}) sources can be studied in enough detail to disentangle the dust emission coming from the region close to the active nuclei from that coming from the remaining host galaxy in the crucial near-IR domain. Also, the number counts in distant samples are dominated by Seyfert luminosity-class sources, and therefore their local properties might be a good representation of the higher redshift counterparts.

All AGNs, whether obscured or not, are thought to harbor a central engine that emits because of the release of gravitational potential energy in an accretion disk surrounding a supermassive black hole. The Unified Model, proposed more than 25 years ago, is still strongly advocated to claim that, in fact, any AGN might look like a Type I source (i.e., unobscured) or Type II source (i.e., obscured), depending on the orientation of the obscuring material, shaped as a torus, with respect to our line of sight (Antonucci 1993). If one assumes that all tori share similar physical traits, then the Unified Model imposes some strong constraints on the observables, such as an expected correlation between the torus orientation angle and the optical depth toward the central source, among others. More recently, a new interpretation has been proposed, where Type I and Type II objects are preferentially drawn from the ends of the distribution of torus covering factor (Elitzur 2012).

The early simple picture of a homogeneous torus (e.g., Pier & Krolik 1992, 1993; Granato & Danese 1994; Efstathiou & Rowan-Robinson 1995), which implied some clear differences in the properties between Type I and Type II sources, has been superseded by more complex models, where a clumpy media, with an overall geometry that still resembles that of a torus, give a much more realistic representation of the obscuring region (Nenkova et al. 2002, 2008a, 2008b; Hönig et al. 2006; Stalevski et al. 2012). Much effort has already been carried out to fit the spectral energy distributions (SEDs) of Type I and Type II AGNs using clumpy distributions of the dusty medium (e.g., Nikutta et al. 2009; Mor et al. 2009; Ramos Almeida et al. 2009, hereafter RA09; Alonso-Herrero et al. 2011, hereafter AH11; Mullaney et al. 2011).

These new prescriptions imply that the correlation between the different observables should be regarded as statistical ones, where individual sources might not be a good representation of the median of a sample. In the same way, the classification such as Type I or Type II also becomes a probabilistic problem. Therefore, samples as large and homogenous as possible must be gathered in order to draw significant results about the torus properties.

With this idea in mind, we have gathered near- and mid-IR observations for a sample of Seyfert II galaxies to determine and fit their SEDs and in this way derive physical and structural parameters of their tori. This paper is organized as follows: Section 2 presents the imaging and spectroscopic observations and their treatment previous to the fitting process; Section 3 presents the CLUMPY models and the fitting procedure; Section 4 presents the obtained results and discusses the best-fit parameters; Section 5 looks into the possible correlations between the results and other characteristics of our sources, such as hydrogen column determined from X-ray data or the presence of a hidden broad-line region (HBLR) inferred from spectropolarimetric observations.

2. OBSERVATIONS

The sample included in this work is formed by all Seyfert II galaxies in the southern hemisphere found in the Extended $12\,\mu$m Galaxy Sample (Rush et al. 1993), comprising 48 Seyfert II galaxies.[5]

The most important characteristic of the $12\,\mu$m Galaxy Sample for this work is that it includes a fairly unbiased sample of nearby ($z \leqslant 0.07$) active galaxies that have been observed in many spectral regimes. It is selected in the mid-infrared (MIR), minimizing possible biases: it includes elliptical, lenticulars, and spiral galaxies (allowing to avoid systematic errors in the decomposition process of the surface brightness profiles, presented in Paper I); it includes a wide range in galaxy inclinations and, most importantly, it includes a wide range of obscuration properties of the nuclear source (allowing a more general test of the nuclear emission models and probing a range of hydrogen columns of $\sim 10^{22}$–10^{25} cm^{-2}).

The Type classification of the objects was obtained from existing catalogs of active galaxies (Veron-Cetty & Veron 1991; Hewitt & Burbidge 1991). Some objects have been re-classified as modern observations have become available. In order to corroborate the classification of the targets, 38 objects were observed with the RC spectrograph on Blanco Telescope in CTIO, in two runs in 2007 August and 2008 February (see below and Paper I).

2.1. Infrared Imaging and Optical Spectroscopy

Details on the imaging observations for our sample are found in Paper I. We presented the near- and mid-IR SEDs for 40 Type II Seyfert galaxies drawn from the Extended $12\,\mu$m Galaxy Sample (Rush et al. 1993), 6 of which had been determined previously by Alonso-Herrero et al. (2003). A detailed account on the data reduction and nuclear flux determination is given in Paper I.

Additionally, optical long-slit data were obtained in order to determine the nature of the nuclear ionizing source and the host

stellar population and are also presented in Paper I. This analysis has shown that three objects from the original sample have H II nuclei (MCG+0-29-23, NGC 6810, and Mrk 897) and therefore have been discarded from any subsequent analysis in this work leaving a total sample of 37 Type II Seyfert nuclei.

2.2. Spectroscopic Observations

2.2.1. Spitzer Data

Most of the galaxies in our sample have been observed using the Infrared Spectrograph (IRS) on board *Spitzer*. The IRS provides moderate-resolution spectroscopy from 5.2 to 38.0 μm. It is composed of four separate modules, with two modules providing $R \sim 60$–120 spectral resolution over 5.2–38.0 μm (the Short-Low or SL, from 5.2 to 14.5 μm; and the Long-Low or LL, from 14.0 to 38.0 μm).

The wide wavelength coverage of IRS spectra can allow a good representation of the mid-IR continuum of Seyfert galaxies. In contrast, $\sim 10\,\mu$m MIR ground-based spectroscopy is normally dominated by polycyclic aromatic hydrocarbon (PAH) features and the 9.7 μm silicate absorption present in that regime, resulting in very little free continuum to be observed.

Results using *Spitzer*/IRS data for nearby Seyfert galaxies have already been published by several authors (Buchanan et al. 2006; Deo et al. 2007; Meléndez et al. 2008; Wu et al. 2009; Thompson et al. 2009; Tommasin et al. 2010). In more detail, Wu et al. (2009) published the spectra for 103 AGNs from the 12 μm Galaxy Sample, of which 44 are in this sample (the remaining 7 lack *Spitzer*/IRS SL spectra). Most of the 44 observations correspond to Program ID 3269 and were obtained between 2004 and 2005, a good match for the timing of our photometry obtained between 2002 and 2004 (see Paper I). The exceptions are IC 5063 and NGC 4941 (PID 30572, observed in 2006 and 2007, respectively), and F 05189−2524 (as part of the IRS calibration campaign).

For those objects observed in mapping mode (all sources in the 3269 program), sky subtraction was performed by differentiating the on- and off-source observations of the same order in each module. In order to isolate the AGN emission from the stellar components, and since rather large apertures were used to obtain the one-dimensional spectra presented by Wu et al. (2009), here we have reprocessed the data in order to have the smallest possible aperture, 2×2 pixels, or 3.6×3.6 arcsec^2 on the sky for the SL module. For data obtained with the IRS staring mode (IC 5063 NGC 4941 and F 0518−2524), the reduction was done in the following manner. Individual pointings to each nod position of the slit were co-added using median averaging. Then on- and off-source images were subtracted to remove the contribution of the sky emission. Spectra from the final two-dimensional images were extracted with a point source extraction mode, which scaled the extraction aperture with wavelength to recover the same fraction of the diffraction-limited instrumental point-spread function (for details, see Wu et al. 2009). Therefore, no "small" aperture spectra are available for these three sources. All the spectra were flux calibrated using the IRS standard star α Lac, for which an accurate template was available.

2.2.2. Star Formation in the Spitzer/IRS Spectra

As the apertures used to extract the *Spitzer*/IRS are larger than the spatial resolution of our photometry and is likely to include extended emission coming from star formation located close to the nucleus, the spectra must be modeled to subtract a
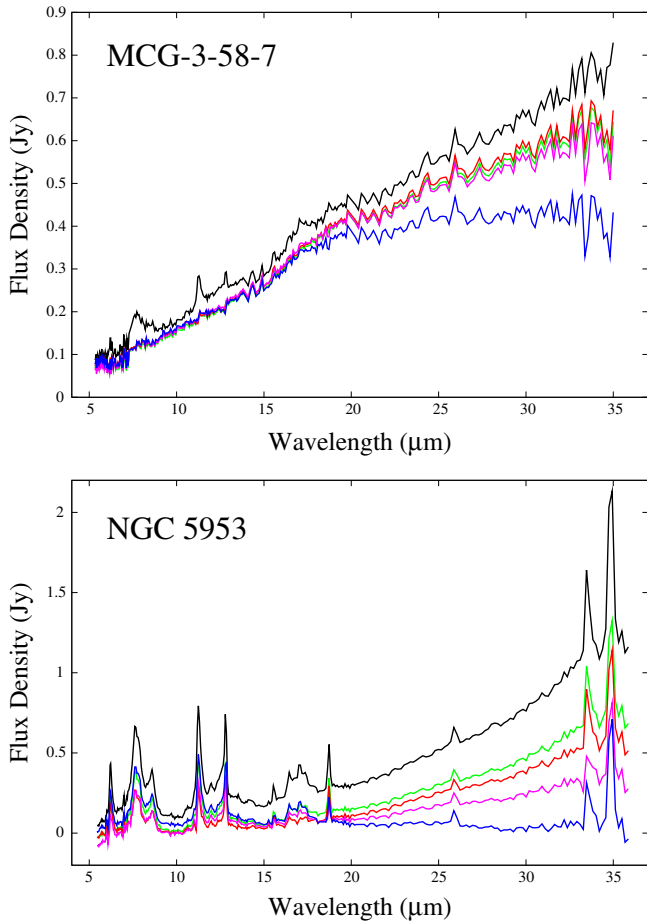
Figure 1. Two extreme examples of subtraction of the emission from star-forming regions using the templates published by Smith et al. (2007). From top to bottom in each panel the curves represent the original *Spitzer*/IRS data obtained using a small extraction aperture (Section 2.2.1) followed by the subtracted spectra using the four templates for star-forming emission. The top panel represents the data for MCG-3-58-7, with a very small star-forming component. The bottom panel represents the data for NGC 5953, which shows strong PAH features even after the subtraction attempts. This object has a very strong circumnuclear star-forming region which clearly is contaminating the *Spitzer* observations.

(A color version of this figure is available in the online journal.)

Figure 2. Examples of star formation corrected *Spitzer*/IRS spectra compared with high-resolution, ground-based, $\sim$8–13 μm T-ReCS data for NGC 5135 and NGC 7130, as published by Díaz-Santos et al. (2010). The *Spitzer* spectra are presented before and after the subtraction of the starburst template and are shown with dotted lines. The subtracted IRS data have been scaled to match the T-ReCS data at $\sim$10 μm.

(A color version of this figure is available in the online journal.)

star-forming component before including the spectra in the nuclear SED of the galaxies in our sample. The presence of PAHs, which dominate the MIR spectra of star-forming regions, will allow to isolate the AGN emission.

Smith et al. (2007) used low-resolution *Spitzer*/IRS spectra of a sample of nearby galaxies spanning a large range in star formation properties to construct four templates in order to account for the differences of the PAH feature strengths and continuum properties. These four templates were used to subtract the star formation component from the MIR spectra of our galaxies. Each template was scaled independently ensuring an optimal subtraction of the PAH features but without oversubtracting the continuum (i.e., without yielding negative fluxes). As can be seen in Figure 18 of Smith et al. (2007), the templates differ the most for $\lambda > 20\,\mu$m. This region was excluded during the model fitting of our SEDs because the lack of photometric data at $\lambda > 10\,\mu$m makes it impossible to determine which template describes best the continuum emission for each particular galaxy for wavelengths longer than 20 μm.

In Figure 1 extreme examples of the subtraction process are shown. The resulting spectra for MCG-3-58-7 have no PAH

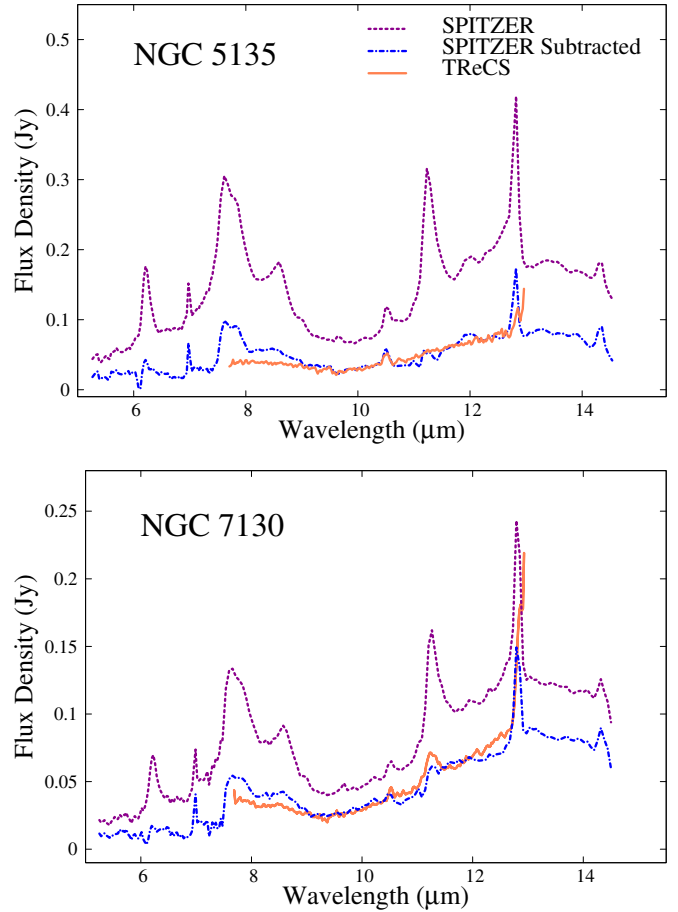features, and the subtraction only modifies the continuum for $\lambda \gtrsim 20\,\mu$m. The second example, NGC 5953, shows strong PAH residuals, indicating that some emission from star-forming regions is still present in the subtracted spectra. As discussed in Paper I, this object has a strong off-nuclear starburst region which is contaminating the *Spitzer* data. Still, for the best subtraction a large fraction of the PAH emission for $\lambda \gtrsim 10\,\mu$m is gone, while the 7.7 μm feature leaves strong residuals. Also, again it can be seen that the main difference between the four different subtracted spectra starts at $\lambda \gtrsim 20\,\mu$m. Only one object in our sample, MCG-2-8-39, did not require any correction for the presence of a star-forming component since no evidence for the presence of PAH emission was found in its spectrum.

We would like to asses the efficiency of our starburst component subtraction procedure. Using high-resolution, ground-based T-ReCS data, Díaz-Santos et al. (2010) have studied the characteristics of the nuclear MIR emission in nearby AGNs. Two objects presented by Díaz-Santos et al. (2010), NGC 5135 and NGC 7130, are also common to our sample.

Figure 2 compares our subtracted *Spitzer*/IRS observations with those obtained from the ground. The *Spitzer* spectra have been scaled so that the subtracted spectrum has a common density flux at $\sim$10 μm with the ground-based data.

Figure 2 shows that a good match is achieved between the *Spitzer*-subtracted spectra and the T-ReCS data, particularly for the regions dominated by the continuum. PAH residuals can be seen for both objects at the position of the 7.7 and 8.6 μm features, even though the ~12–13 μm region presents a very clean subtraction. We can tentatively conclude that whenever a good subtraction of the PAH features is achieved, the resulting spectrum can provide a good representation of the emission from the active nucleus. In fact, to avoid being too sensitive to a poor subtraction, whenever PAH residuals are seen, we use only a few spectral windows of the *Spitzer* observations to constrain our model fitting (Section 4.1). It must be stressed, however, that PAH and dust emission are not the only components present in the MIR spectra of starbursts. Silicate absorption can be seen toward starburst nuclei with a mean flux ratio of the local continuum to the base of the line of 0.2 ± 0.1.

In particular, NGC 1144, NGC 5135, NGC 5953, NGC 7130, NGC 7496, and NGC 7582 show a strong starburst component before the template subtraction, and significant structure afterward. For NGC 1144 a clean PAH subtraction is achieved, but because of the intrinsic silicate absorption toward starburst nuclei just mentioned, it is impossible to asses whether or not the residual dip seen at ~10 μm is due to the presence of a dusty torus. NGC 7582 shows some PAH residuals at the position of the 7.7 μm PAH feature after the template subtraction, and therefore, again it is not simple to asses the presence of the residual 10 μm feature. However, results from small aperture, ground-based spectroscopy of NGC 7582 show that in this case the presence of the silicate absorption is related to the nuclear source (AH11).

2.2.3. Other Spectroscopic Data

NGC 1068 was observed with the *Infrared Space Observatory* (*ISO*) satellite in 2001, and its spectrum was published by Le Floc'h et al. (2001), already divided into AGNs and starburst components. Our photometry for this galaxy comes from an earlier date (1998 and 1999), but IR variability of this nucleus was of the order of 0.1 mag in the *K* band during that period (Taranova & Shenavrin 2006).

NGC 7172 was observed using the T-ReCS spectrograph mounted on the Gemini South telescope (Roche et al. 2007). Therefore, this spectrum presents a narrower spectral coverage than the space-borne observations. Because of the high spatial resolution, this spectrum isolates the AGN emission from the active nucleus.

3. MODELING THE NUCLEAR IR SEDs

3.1. Clumpy Torus Model

As was suggested in many previous works, a clumpy structure of the distribution of gas and dust in the torus is more realistic than a continuous one. The fundamental difference between clumpy and continuous density distributions is that radiation can propagate freely between different regions of a medium populated by optically thick clouds when it is clumpy, implying that cold dust may exist near the nucleus, and dust directly illuminated by the central source may exist far from it. The difficulties in modeling such an environment plus the time-consuming calculations (and technical limitations) prevented the developing of such approaching until recently.

Nenkova et al. (2002) were the first to study a clumpy distribution for the gas and dust in the torus. Nenkova et al.

(2008a) presented the general formalism for handling this clumpy media. The resulting SEDs (hereafter the CLUMPY models) were presented in Nenkova et al. (2008b), with an erratum on their calculations in Nenkova et al. (2010). They assume that all the clouds are identical and characterize each one by its size (which should be much smaller than the separation between clouds), its opacity, and its spatial distribution (the angular distribution of the clouds). Also, the different dust temperatures in the illuminated surface and the dark side of the cloud are accounted for. The size distribution of the dust grains is that described by Mathis et al. (1977), composed by the standard Galactic mixture (53% of silicate and 47% of graphite). Scattering is taken into account, dominating at short wavelengths ($\lambda \lesssim 1\,\mu$m). They argue that the illuminating spectrum makes no difference at wavelengths dominated by dust emission, $\lambda \gtrsim 2$–3 μm, but at shorter wavelengths the AGN scattered radiation dominates.

Through the clumpy treatment, Nenkova et al. (2002) can naturally explain the rather low and diverse dust temperatures found close to the nucleus of NGC 1068 (Jaffe et al. 2004; Schartmann et al. 2005). Furthermore, it is found that the X-ray attenuating column density is widely scattered around the column density that characterizes the IR emission, because the IR flux is collected from the entire observed area (averaging over all the clouds), while the X-ray opacity is calculated from one particular line of sight.

The parameters for the CLUMPY models are the optical opacity of each cloud (τ_V), the number of clouds through the torus equator ($\mathcal{N}_0$), the angular and radial distribution of the clouds (σ, measured from the torus equator, and r^q, respectively), $Y = R_{\mathrm{out}}/R_{\mathrm{in}}$, and the angle between the axis of symmetry of the system and the line of sight ($\angle i$). The values for each parameter are shown in Table 1.

Essentially, the characteristics of the emerging emission depend on whether the IR photons originate on the side of a cloud that is directly illuminated by the AGN, or the region that is heated by the radiation emitted by other clouds, the dark side. The optical depth will determine how different the SEDs of these individual clouds are. The number of clouds of the whole torus population and their geometrical distribution will determine how many clouds are in the shadows of other clouds, while our orientation with respect to the torus will dictate how much of directly illuminated or dark parts of clouds we see.

3.2. Two-phase Torus Models

Very recently, Stalevski et al. (2012) have proposed two-phase models where dust might not only be found in clumps or clouds, but also in a diffuse medium filling the space between the clumps (hereafter the 2pC models). The diffuse medium is controlled by two parameters: the filling factor and contrast (see Table 1). The filling factor determines the statistical frequency of clumps, with a value $\gtrsim 0.25$ yielding enough clumps to form an interconnected, sponge-like structure. The contrast parameter determines what fraction of the dust is found in the clouds, with a value of 1 corresponding to a smooth distribution and a value >1000 having effectively all the dust in the clumps.

Stalevski et al. (2012) claim that the largest differences when this diffuse medium is included can be seen as a larger flux output in the near-IR.

Table 1
Parameter Values for Torus Models

Par	Values	Description
CLUMPY models (as described in Nenkova et al. 2008b)		
τ	5, 10, 20, 30, 40, 60, 80, 100, 150	V-band optical depth of individual clouds
$\mathcal{N}_0$	1–15 in steps of 1	Number of clouds at torus equator
σ	15–70 in steps of 5	Torus half-opening angle (0 at equator)
q	0–3 in steps of 0.5	Radial cloud distribution exponent
Y	5, 10–100 in steps of 10	Torus thickness ($= R_{out}/R_{in}$)
$\angle i$	0–90 in steps of 10	Viewing angle (0 at polar axis)
2pC models (as described in Stalevski et al. 2012)		
$\tau_{9.7}$	0.1, 1, 5, 10, 15, 20	Total 9.7 μm optical depth at equator
R_{in}	0.5	Torus inner radius in pc
R_{out}	15	Torus outer radius in pc
p	0, 1	Radial clump distribution exponent
q	0, 2, 4, 6	Polar clump distribution exponent
Θ	50	Torus half-opening angle (0 at equator)
Inclination, i	0, 40–90 in steps of 10	Viewing angle (0 at polar axis)
Filling factor[a]	0.15, 0.25	Frequency of clumps
Contrast	100	Fraction of dust in clumps
Clump size[a]	0.15, 1.2	In pc
Resolution[a]	$1 \times 1 \times 1$, $8 \times 8 \times 8$	Number of grid cells per clump

Note. [a] Available parameter combinations are filling factor of 0.15, size clump of 0.15 pc, and resolution of $1 \times 1 \times 1$; or filling factor of 0.25, size clump of 1.2 pc, and resolution of $8 \times 8 \times 8$.

3.3. Fitting Procedure

3.3.1. χ^2 Test

We compare our observed SEDs with models where the torus is described as a clumpy distribution of gas and dust as proposed by Nenkova et al. (2008a, 2008b), and which also includes a diffuse component as proposed by Stalevski et al. (2012).

In order to include the *Spitzer* data in the modeling, we had to take into account the scaling of the spectra, the spectral windows to be used, and the associated errors.

For those objects where we had an N-band flux measurement, the spectra was scaled to match the photometric value. For those objects without a measurement, the average of the scaling factors found for the objects with N-band photometry was used. This was found to be $\sim$0.06 $\pm$ 0.03, with the error corresponding to the standard deviation of the determined scaling factors. Photometric upper limits are also shown in the SEDs, but they were not used during the fitting process.

To avoid using *Spitzer* spectra with a poor subtraction of the starburst component, we masked out strong PAH residuals during our fitting procedure, Also, for very noisy spectral data, the windows were averaged into "photometric" points, assuming the corresponding error of the N-band measurement. For well-subtracted, high signal-to-noise spectra, the whole spectrum was used during the model fitting. We assumed a 5% error for each spectroscopic point (Wu et al. 2009) of the *Spitzer* observations.

We programmed a simple χ^2 routine that calculates the scaling factor needed shift the clumpy torus models to match the observed SEDs. The best fits correspond to the smaller χ^2 values. Note that given our adopted scaling for the *Spitzer* data, the determined χ^2 do not necessarily represent the actual goodness of the fit but allows to determine which is the best possible model.

Some fits obtained using the CLUMPY library, however, are at odds with the expected results. For example, the canonical Seyfert II galaxy NGC 1068, which has a well-constrained SED, including a large number of IR photometric observations and a well-determined MIR spectrum, is best fitted by models presenting a small value of the torus angle, that is, models with face-on orientations. This is not supported by a large body of evidence on the geometry of the central region in this object. In fact, based on this evidence, AH11 restricted the torus angle to values corresponding to high inclination only.

It can be concluded that the shape of the SED alone might not be sufficient to distinguish between models in the very large CLUMPY library. Whether or not a similar situation would be found when using the 2pC models is not clear due to the much smaller set of available models.

3.3.2. L^{bol} Estimates: Breaking the Degeneracy

In order to break the possible degeneracy between different CLUMPY models that present similarly shaped SEDs in the near- and mid-IR regime, we have introduced another restriction. Different physical parameters or geometry of the CLUMPY models, scaled to the same flux level, will necessarily imply different bolometric luminosities of the central AGN. Therefore, we can use the "observed" bolometric luminosities to discriminate between competing models. This is similar to the approach followed by Mor et al. (2009) when modeling *Spitzer* observations of 26 luminous quasars.

Determining the bolometric luminosity of Type II sources is not straightforward. The two most promising luminosity proxies are the [O III] line emission arising from the narrow-line region (NLR), and the 2–10 keV emission in the X-rays. However, both methods present important drawbacks. [O III] fluxes can be difficult to correct for slit losses and aperture effects for very extended NLRs, while determining an accurate extinction correction can be problematic when the Balmer decrement is affected by absorption line features from the underlying stellar population. Probably of less importance would be taking into account the fraction of UV flux intercepted by the putative torus, and determining the contamination by a starburst component.

At the same time, the 2–10 keV emission is strictly a proxy only for Compton-thin sources (i.e., those with $N_H < 10^{24}$ cm^{-2}), and determining accurate unabsorbed 2–10 keV fluxes can be difficult for highly absorbed sources ($N_H \sim 10^{23}$–10^{34} cm^{-2}) with average quality data. See the work by LaMassa et al. (2010) for further discussion on the subject of luminosity proxies.

We have compiled extinction- and absorption-corrected [O III] and 2–10 keV fluxes for our sample (Table 2). [O III] measurements are available for all of our sources, and it can be seen that they generally agree within a factor of three or better. X-ray fluxes are only available for about 40% of the sample, mainly due to the fraction of Compton-thick sources.

Using the expressions derived by Marconi et al. (2004), we have estimated the bolometric luminosities from the 2–10 keV X-ray observations (see Table 2). For the [O III] data, we have followed the work of Lamastra et al. (2009), who compared extinction-corrected [O III] luminosities and 2–10 keV fluxes for a sample of Type II Seyfert galaxies to find $L_{2-10\,\mathrm{keV}} \approx 10\,L_{\mathrm{O\,III}}$. Adopting the Marconi et al. (2004) bolometric correction for the X-ray data, Lamastra et al. (2009) then tabulated three different bolometric corrections for $\log(L_{\mathrm{O\,III}})$ in the ranges 38–40, 40–42, and 42–44 erg s^{-1}. Instead, we have combined the [O III] versus 2–10 keV correlation given above with the bolometric correction found in Marconi et al. (2004) to find the cubic expression:

$$\log L_{\mathrm{O\,III}}/L_{\odot} = 9.45 - 0.76\mathcal{L} + 0.012\mathcal{L}^2 - 0.0015\mathcal{L}^3, \quad (1)$$

with $\mathcal{L} = \log L^{\mathrm{bol}}/L_{\odot} - 12$. The results are reported in Table 2 where we give the average value of L^{bol} when more than one [O III] flux is available. From objects with multiple [O III] observations we find an rms of 0.3 ± 0.05 in fractional flux. This rms value will be used as the standard deviation of the [O III] flux distribution in what follows.

Table 2 shows that when both estimates of the bolometric luminosities are available, in about 50% of the cases the values agree within a factor of five or better. However, in the other 50% of the cases there are important disagreements. It is significant that in all but two cases (NGC 1144 and NGC 7172) $L^{\mathrm{bol}}_{\mathrm{O\,III}} > L^{\mathrm{bol}}_{2-10\,\mathrm{keV}}$, may be due to an insufficient absorption correction of the X-ray flux since several of these sources have large absorbing columns. Because of this, and the complete availability of [O III] fluxes for our sample, we will use $L^{\mathrm{bol}}_{\mathrm{O\,III}}$ as a prior for the bolometric luminosity of our sources.

From the models, the bolometric luminosity of the AGN illuminating the torus is found as $L^{\mathrm{bol}}_{\mathrm{model}} = \Theta \times 4\pi d^2$, where d is the distance to the galaxy and Θ is the scaling factor needed to shift the model to the observed SED data points.

We use $L^{\mathrm{bol}}_{\mathrm{model}}$ to restrict the best-fit models by applying a Bayesian approach. We compute prob(model|SED) $\propto$ prob(SED|model)×prob(model|Lbol), where we assume prob(SED|model) $\propto \exp{-(\chi^2/2)}$ (i.e., the likelihood that the SED has been obtained from the model) and prob(model|Lbol) $\propto \exp(-(L^{\mathrm{bol}}_{\mathrm{O\,III}} - L^{\mathrm{bol}}_{\mathrm{model}})^2/2\sigma^2_{\mathrm{O\,III}})$ as prior, with $\sigma_{\mathrm{O\,III}} = 0.3 \times L^{\mathrm{bol}}_{\mathrm{O\,III}}$.

Figure 3 shows the case study for NGC 1068. When restricting $L^{\mathrm{bol}}_{\mathrm{model}}$ to the value implied by the observed [O III] fluxes, the correct picture emerges. When applied to the entire sample, we find that about ~20%–25% of the sources change significantly their best-fit model results when applying the L^{bol} restriction.

3.3.3. Fitting Sources with Near-IR Excess

In many of our sources a near-IR excess is observed. These SEDs turn upward for $\lambda \lesssim 3\,\mu$m, that is, they present an index
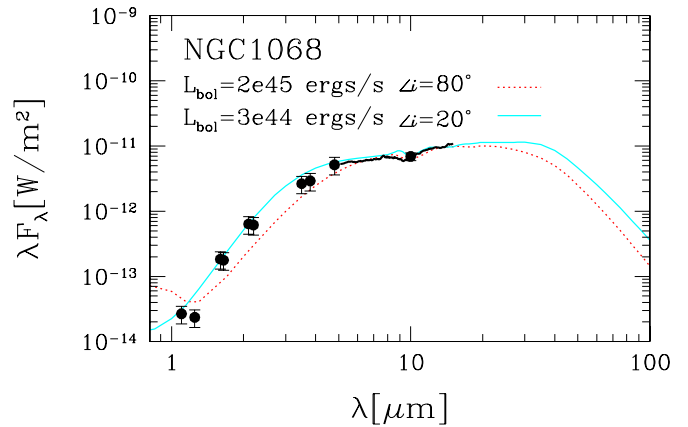

Figure 3. Fits to the SED of NGC 1068 with and without (dashed and continuous lines, respectively) a L^{bol} prior (see Section 3.3.2 for details).
(A color version of this figure is available in the online journal.)

$\alpha < 1$ in the near-IR at a 1σ level (for $\lambda f_\lambda \propto \lambda^\alpha$). These objects are flagged in Table 2. Note that MCG+0-29-23, NGC 6810, and Mrk 897, which are classified as star-forming nuclei and therefore are not included in the present analysis, also show a near-IR excess (Paper I). Also, NGC 34 and NGC 5953 have $\alpha < 1$ (although NGC 34 is not at a 1σ level), but as argued below (see also Section 4.1), it is very likely that these sources are contaminated by a starburst component and therefore are not flagged in Table 2 as presenting a "genuine" near-IR excess.

In Paper I, several possibilities to explain the presence of the observed near-IR excess were proposed: contribution from a compact nuclear starburst or a nuclear stellar cluster, emission from the accretion disk, emission from a compact jet, or emission from a very hot dust component that survives within the sublimation radius of the torus.

The first scenario, the contribution from a compact starburst, was not supported by the analysis of diagnostic diagrams from emission-line ratios and the analysis of the observed stellar continuum (see Paper I). Strong PAH residuals in the *Spitzer* data do not necessarily imply a strong nuclear starburst component because of the large apertures. However, the nuclear optical spectra presented in Paper I suggests that NGC 34 might have a strong nuclear starburst, while NGC 5953 has a very strong circumnuclear star-forming region.

A second scenario is the presence of a luminous nuclear stellar cluster. While nuclear clusters are found in most galaxy nuclei and are characterized by a light weighted stellar age of $\sim 10^8$–10^9 years (Walcher et al. 2006), their luminosities (absolute magnitude $z_{AB} = -13$ for the most luminous cases; Côté et al. 2006) are not sufficient to make a significant contribution to the observed near-IR fluxes in our sample.

The last three scenarios would require the leaking of the radiation from the central region through the clumpy obscuring torus. Since the nature of a clumpy medium would allow for certain lines of sight to peer directly at the central engine, even for highly obscured sources, in what follows we will study these scenarios in more detail. As 12/31 sources show evidence for a near-IR excess, we can postulate that the clumpy structure leaves, on average, ~40% of the lines of sight free of absorption for Type II sources.

The first working hypothesis is that the presence of a near-IR excess could be due to central disk emission piercing through the torus for the particular line of sight we have of the system. To test this hypothesis, SED fitting was done using the whole library

Table 2
Compiled Data for Our Sample

Galaxy[a]	Class[b]	HBLR[c]	BD[b]	$F_{O\,III}^c$ [d]	$F_{2-10\,keV}^c$ [d]	$L_{O\,III}^{bol}$	$L_{2-10\,keV}^{bol}$	$\log(N_H)$ [d]	$F_{5-8\,GHz}$ [e]	R_L [f]	α [g]
				(10^{-12} erg seg^{-1} cm^{-2})		(erg s^{-1})	(erg s^{-1})	(cm^{-2})	(mJy)		
(1)	(2)	(3)	(4)	(5)	(6)	(7)	(8)	(9)	(10)	(11)	(12)
NGC 34	Sy2–H II	N	13.7	1.0–1.3	...	44.2	...	>24⟨	14.5	4.7	0.97 ± 1.26
F 00198−7926 N	Sy2	N	...	0.1–0.4	...	44.9	...	>24⟨	...	...	0.10 ± 0.15⟨
F 00198−7926 S	Sy2	N	...	0.1–0.4	...	44.9	...	>24⟨	...	...	5.02 ± 0.16
F 00521−7054	Sy2	N	8.3:	0.6–1.3	...	45.5	...	...	...	...	1.69 ± 0.28
ESO 541-IG012	Sy2	...	6.1:	0.5	...	44.9	...	...	0.8	0.4	2.28 ± 0.62
F 01475−0740	Sy2	Y	7.1	0.8–0.9	0.8	44.0	42.7	21.6	130	70	0.34 ± 0.09⟨
NGC 1068	Sy2	Y	...	98–190–280	...	45.3	...	>25⟨	1342	1.2	5.77 ± 0.86
NGC 1144	Sy2	N	...	0.1–0.3–0.5	...	43.9	44.9	23.8	2.3	3.4	−0.67 ± 0.24⟨
MCG-2-8-39	Sy2	Y	4.2	0.1–0.2–0.7	2.7	44.2	43.9	23.5	<0.3	<0.2	−1.00 ± 0.01⟨
NGC 1194	Sy2	...	6.6	0.3	10.9	43.1	43.8	24.0	0.9	2.6	5.92 ± 0.43
NGC 1320	Sy2	N	3.8	0.3–0.5–0.6	...	43.0	...	>24⟨	1.0	2.1	2.86 ± 0.17
F 04385−0828	Sy2	Y	4.0:	0.04–0.09	2.4–6.0	42.5	43.3	...	6.0	132	3.43 ± 0.64
ESO 33-G2	Sy2	...	5.0:	0.6	...	43.8	...	22.0	...	...	2.86 ± 0.68
F 05189−2524	Sy2	Y	...	0.8–1.2–1.3	4.3–6.4	45.1	44.6	22.8	6.9	1.2	2.57 ± 0.66
NGC 3660	Sy2	N	3.3:	0.6–1.0	2.3	43.4	42.9	20.5	0.8	0.9	−0.32 ± 0.37⟨
NGC 4388	Sy2–SB	Y	4.0	1.1–2.8–4.5–4.8	43.0	43.9	44.0	23.4	34.6	4.9	4.18 ± 2.17
NGC 4501	Sy2	N	3.7:	0.06–0.07	0.02	41.8	40.2	22.2	2.6	95	−0.93 ± 0.11⟨
TOL 1238−364	Sy2	Y	4.0	1.2–2.8–3.4	...	44.0	...	>24⟨	2.3	0.4	−0.46 ± 0.02⟨
NGC 4941	Sy2	N	4.6	1.1–3.6–4.6	3.0	43.0	41.8	23.7	9.0	2.7	...
NGC 4968	Sy2	...	4.3	0.4–0.7	...	43.1	...	>24⟨	2.1	3.3	5.32 ± 0.01
MCG-3-34-64	Sy1.8	Y	...	4.2–5.2	4.0	44.8	43.6	23.6	42.2	2.2	−0.14 ± 0.19⟨
NGC 5135	Sy2–H II	N	5.6	1.4–2.3–2.4	...	44.2	...	>24⟨	<2.3	<0.4	3.16 ± 2.08
NGC 5506	Sy1.5–1.9	N	4.4	1.8–1.9–5.5–5.7	58–108	43.6	44.1	22.5–20.4	67.6	11.9	2.83 ± 0.80
NGC 5953	LINER–Sy2	...	4.2	0.2–0.7	...	42.6	...	...	1.1	3.1	−1.68 ± 1.53
NGC 5995	Sy2–H II	Y	...	6.6–18.1	...	45.9	42.5	21.9	2.4	...	1.65 ± 0.10
F 15480−0344	Sy2	Y	4.6:	2.2–2.6–5.0	...	45.3	...	>24⟨	12.4	0.6	0.50 ± 0.23⟨
NGC 6890	Sy2	N	5.0	0.5–0.6–0.7	...	43.0	...	...	0.5	0.8	1.89 ± 0.92
IC 5063	Sy2	Y	...	3.5–6.5	12–30	44.4	44.0	23.4	506	31.8	−0.37 ± 4.00
NGC 7130	LINER	N	7.9	2.1–4.5–6.0	...	44.7	...	>24⟨	18.1	1.1	−0.08 ± 0.33⟨
NGC 7172	Sy2–H II	N	...	0.04–0.07	21	41.9	43.7	22.9	4.7	259	...
MCG-3-58-7	Sy2	Y	4.7	0.7–1.5	2.3	44.7	43.9	23.4	0.5	0.1	2.42 ± 0.35
NGC 7496	Sy2–H II	N	5.1	0.1–0.1–0.3–0.5	...	42.0	...	22.7	3.8	32.2	0.39 ± 0.24⟨
NGC 7582	Sy2	N	...	1.6–2.8–3.8	4.0–27.2	43.3	42.3	23.1	51.8	14.2	2.66 ± 0.31
NGC 7590	Sy2–H II	N	5.9	0.2–0.2	1.2–1.14	42.0	41.8	<21	<0.2	<2.2	...
NGC 7674	Sy1–H II	Y	...	1.2–1.6–1.7–1.9	...	44.8	...	>25⟨	12.8	1.9	3.04 ± 0.54
CGCG 381−051	H II	...	...	0.2	...	43.6	...	...	0.6	2.4	−0.27 ± 0.20⟨

Notes. [a] For alternative galaxy names, see Paper I. [b] Spectral class and Balmer decrements (BD) from Paper I; unreliable BD values are labeled with ":". [c] Compilation of HBLR taken from Shu et al. (2007). [d] Data from Bassani et al. (1999), Brightman & Nandra (2008), Greenhill et al. (2008), Noguchi et al. (2010), Panessa & Bassani (2002), Sazonov et al. (2007), Shu et al. (2007), Tran (2003), and Winter et al. (2008); only direct X-ray flux components are quoted; ⟨ indicates Compton-thick sources. [e] Data from Thean et al. (2000) and Gallimore et al. (2006) at 8.4 and 5 GHz, respectively; radio flux for IC 5063 at 5 GHz was obtained from Gregory et al. (1994). [f] $R_L \equiv f_B/f_{5\,GHz}$ (see the text for details). [g] Near-IR slopes from Paper I; values of $\alpha < 1$ at a 1σ level are flagged with a ⟨.

of CLUMPY models, which, besides the pure torus emission, also have "SED+AGN" models, in which a torus is combined with the emission from the central nucleus. The advantage of using these models to simply adding an arbitrary power-law component is that the normalization of the AGN emission, which in turn illuminates the obscuring torus, is treated consistently with that of the emission from the torus itself.

A consistency check to the best-fit "SED+AGN" models is to test whether the accretion disk emission is expected to be seen in the optical, since our sample is characterized by a strong optical stellar continuum and the lack of a power-law component. We find that only three sources require a moderate amount of reddening ($A_V \lesssim 1$) to prevent disk emission from showing in the optical observed spectra (see Figure 4). This extinction could correspond to lines of sight at a grazing angle to some clouds in the torus, or to extinction introduced at larger scales. In principle, therefore, it is possible to have a disk component

appearing at near-IR wavelengths without a disagreement with the optical observed continuum.

A second consistency check is to examine the observed hydrogen column densities. A direct view of the accretion disk should correspond to objects presenting small X-ray inferred hydrogen columns, since these two observations would probe the line of sight to the central region of the active nucleus. Of the 12 sources identified as having a near-IR excess, 1 lacks X-ray observations (CGCG 381−051). Of the remaining, eight have fairly large absorbing columns ($\log(N_H) \gtrsim 22.5$ cm^{-2}; see Table 2), while IRAS 01475−0740, NGC 3660, and NGC 4501 have $\log(N_H) = 21.6$, 20.5, and 22.2 cm^{-2}, respectively.

This result could be explained in the context of a clumpy torus if the probability of the power-law emitting region being obscured would be lower by ~70% (8/11) than that of the X-ray emitting region. In fact, in the canonical picture of the central engine of an AGN, the X-ray emitting region probably
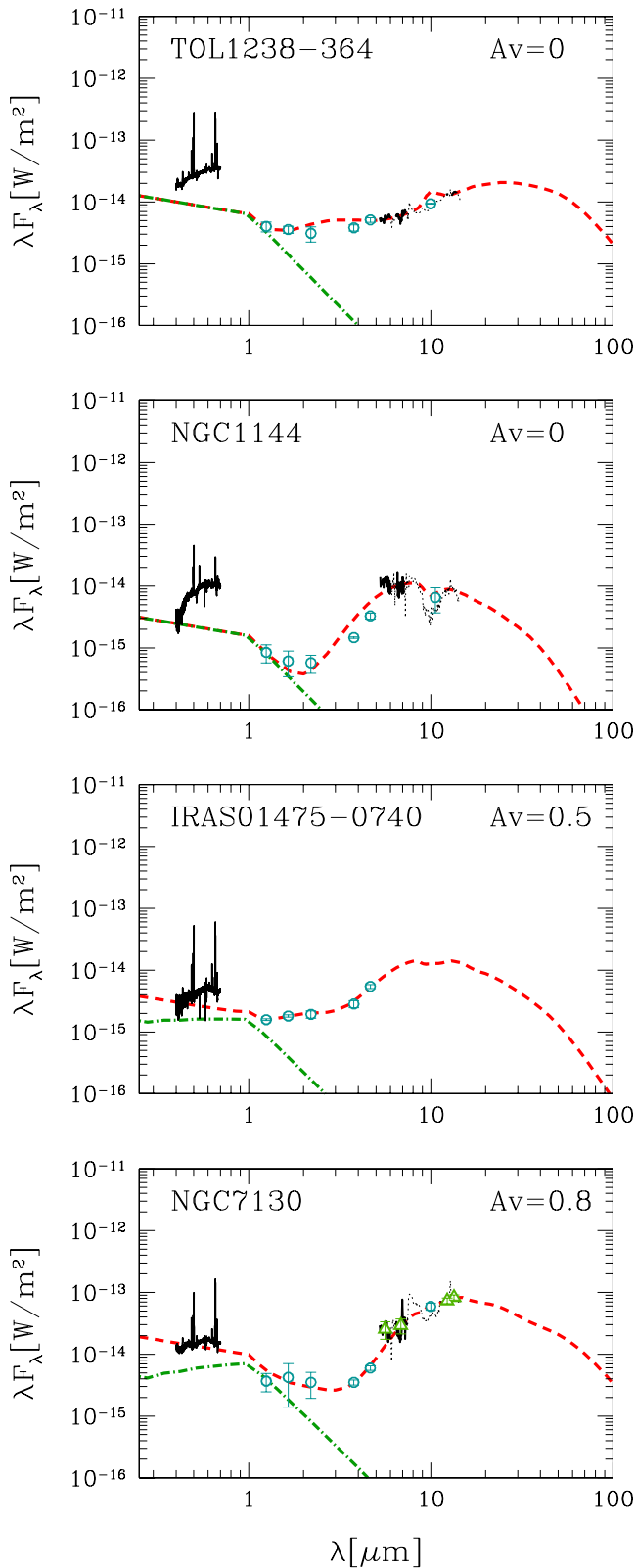
Figure 4. Example nuclear infrared SEDs and optical spectra from Paper I for four of our sources with near-IR excess. The best model fit to the infrared SED is shown together with the accretion disk component after extinction has been applied to prevent it from appearing in the optical regime (dashed and dash-dotted lines, respectively). The amount of extinction applied to the accretion disk is shown at the top-left corner of each panel. Note that only TOL 1238−364 was observed under photometric conditions (Paper I), implying that the absolute flux calibration of the optical spectra for NGC 1144, IRAS 01475−0740, and NGC 7130 might be underestimated.

(A color version of this figure is available in the online journal.)

does not extend further than a few gravitational radii from the central black hole, while the optically emission coming from the accretion disk should reside hundreds of gravitational radii away, if a classical Shakura–Sunyaev α-disk is adopted (Shakura & Sunyaev 1976).

However, this argument should also work in the opposite sense: those sources with small values of N_H should show a high probability to also exhibit an accretion disk component in the optical and near-IR. From Table 2 we find that, besides IRAS 01475−0740, NGC 3660, and NGC 4501, four other galaxies that do not show a near-IR excess have $N_H \lesssim 22$ cm^{-2}: ESO 33-G2, NGC 5506, NGC 5995, and NGC 7590. In summary, out of seven sources with low N_H columns, three have near-IR excess and four do not. Hence, there is a ∼50% chance to have a direct view toward the accretion disk when there seems to be unimpaired access of the innermost region toward the central black hole. This result comes from small number statistics but still argues against our null hypothesis.

Moreover, our sample is composed entirely by objects with Type II classification from the absence of broad emission lines in their optical spectra, that is, their broad-line region (BLR) is to a large degree completely obscured to us in direct light. But from the analysis above, in ∼40% of the sources we might have a direct view of the accretion disk. As before, this would suggest that the probability of seeing a larger structure is smaller than that of seeing more compact regions. This strongly argues against the interpretation of the near-IR excess as emission from the accretion disk. It is still feasible that in some of our sources the accretion disk component is indeed seen in direct emission, but it seems very unlikely that this can explain the large fraction of sources with near-IR excess in our sample. Moreover, as it will be further discussed in Section 4.3, other works have already claimed the presence of an extra near-IR component in the SEDs of Type I AGNs, where the accretion disk and the innermost torus is readily visible. That is, the component is required *besides* the disk and torus emission, as modeled by CLUMPY. This extra component has so far been accounted for using a blackbody spectrum.

Consequently, we conducted a fitting process using the torus CLUMPY "SED" models plus a blackbody component with a free scaling parameter (as opposite to the previous "SED+AGN" modeling where both components were jointly scaled), representing emission from a hot component such as hot carbonaceous dust grains surviving within the sublimation radius of the silicate dust. We tested temperatures in the 1000–2500 K range using steps of 100 K.

The models proposed by Stalevski et al. (2012) might offer a different solution. Hot dust located in the diffuse component might be found further out in the torus and therefore increase the chance of making a contribution to the near-IR even for Type II sources. Because of the much smaller library of 2pC models currently available, and to test whether the treatment of the diffuse component detailed in Stalevski et al. (2012) can account for the near-IR excess emission, we conducted a simple χ^2 minimization without adding extra components.

3.3.4. Fitting Radio-loud Sources

We have compiled nuclear radio measurements for most of our sources from Thean et al. (2000) and Gallimore et al. (2006) at 8.4 and 5 GHz, respectively (see Table 2). We computed a radio-loudness parameter as $R_L = F_{5\,GHz}/F_B$ as defined by Kellermann et al. (1989). Thean et al. (2000) fluxes were taken to 5 GHz assuming $S_\nu \propto \nu^{-0.2}$, implying a correction factor

of 1.1 for these measurements. Since we do not have a direct measurement of the nuclear B magnitudes, we have used the $L_{O\,III}^{bol}$ values found in Table 2 to determine B fluxes assuming the relation defined by Marconi et al. (2004). Radio-loud AGNs are defined as those with $R_L \gtrsim 30$. We can see that five of our sources fulfill these criteria, while most are in the radio-quiet regime ($R_L \ll 10$).

As detailed in Paper I, 3/12 of the sources with near-IR excess are classified as radio-loud: IRAS 01475−0740, NGC 4501, and NGC 7496. We can try to estimate whether Synchrotron emission is responsible for the near-IR excess using a correlation between optical and radio flux determined for unbeamed low-power radio-loud AGNs derived by Chiaberge et al. (1999) after interpolating to the J-band wavelength.

The predicted fluxes for our sources are extremely small, between five and seven orders of magnitude below the observed fluxes, and clearly will not explain the observed near-IR excess, unless strong beaming takes place. We cannot rule out this last possibility. Radio variability would uncover beamed sources.

We conducted the fitting process for the three candidate beamed radio sources using the torus CLUMPY "SED" models plus a power law with a free scaling parameter. The power law would correspond to a beamed jet which can have strong near-IR emission during a "high-state" (Bonning et al. 2009).

We used the calculated near-IR slopes as a first guess and explored 10 values around α in steps of 0.1.

3.3.5. Fitting Sources with Strong Silicate Absorption

A few of our sources present significant silicate absorption at 9.7 μm while showing strong near-IR emission, that is, showing a "broad" SED. The most extreme silicate absorption features are seen in NGC 7172 and NGC 7582, while NGC 1194, IRAS 04385−0828, NGC 4388, and NGC 5506 correspond to more moderate cases.

Using S_{10} to quantity the depth of the silicate feature ($S_{10} = \ln F_\lambda / F_{c,\lambda}$, where F_λ corresponds to the flux at the deepest point of the absorption feature and $F_{c,\lambda}$ corresponds to the flux in the interpolated continuum) we find that NGC 7172 and NGC 7582 have $S_{10} \sim -2.0$ and ~ -1.4, respectively, while the other four sources listed above have S_{10} values between ~ -0.7 and -1.

We find that it is not possible to properly fit NGC 5506, NGC 7172, and NGC 7582 with the set of current CLUMPY models because a combination of deep silicate absorption and SEDs with strong near-IR emission is not available. Even though NGC 5506 has a moderate absorption feature, it has a particularly broad SED and therefore the obtained fits are poor.

This is because CLUMPY models can only produce $S_{10} \gtrsim -1$ for intermediate optical depths, large number of clouds and edge-on lines of sight. At the same time, a large number of clouds yield models with a pronounced decrease in flux below 20 μm, as can be seen in Figure 6 of Nenkova et al. (2008b), therefore producing "narrow" SEDs. This issue is seen in the fits performed by AH11 to NGC 5506, NGC 7172, and NGC 7582 (note that we share common photometry with AH11 for NGC 5506 and NGC 7172). From their Figure 6 it is clear how the fits to NGC 5506 and NGC 7582 become much steeper in the near-IR once the spectral information from the silicate absorption is taken into account. Only Circinus in Figure 5 of AH11 presents a combination of SED shape and silicate absorption strength compatible with the models.

On the other hand, Stalevski et al. (2012) show that their 2pC models can have a value of S_{10} as low as −2.4. Crucially, their diffuse torus component contributes more significantly to the

near-IR spectral range than the CLUMPY models, producing "broader" SEDs. However, as noted by Stalevski et al. (2012), this effect is more substantial for face-on orientations, while we expect that a large fraction of our sources prefer edge-on orientations.

Levenson et al. (2007) have argued that a deep silicate absorption feature can be obtained if the emission source is deeply embedded in an optically and geometrically thick dusty structure. This is a reminiscence of the old continuous torus models, with the consequence that broad SEDs are not recovered. Alternatively, deep silicate absorption can be introduced by a thick screen of cold dust located further away from the central source, as proposed by AH11. Given the rather small expected torus sizes, it is possible that an external screen of dust will introduce the absorption feature along the line of sight toward us. However, as before, this screen will also reprocess the near-IR emission into longer wavelengths, and therefore the final SED will look narrower that the observations.

We used DUSTY (Ivezić et al. 1999) to explore further this scenario using CLUMPY torus models as the incident spectrum on a slab of cold or hot dust. We found that an SED with strong near-IR emission is only recovered when the temperature of the slab is as high as ∼1000 K and for moderate optical depths. However, this combination of parameters essentially retains the silicate feature of the incident spectrum ($\tau_V \sim 20$ implies $\tau_{9.7} \sim 1$), while adding the emission from the screen of hot dust to the near-IR range. Essentially, this corresponds to a scenario where enough hot dust is added to the SED to increase its near-IR output without significantly altering the torus emission in the mid-IR. This can be regarded as an analogous model to the one proposed in Section 3.3.3 to explain the upturn in the near-IR emission of many of our sources. Note that although this scenario might seem similar to that proposed by Stalevski et al. (2012), our added blackbody component is completely arbitrary and has no physical connection to the torus structure.

In summary, we finally conducted the fitting to sources with deep silicate absorption and a broad SED as described previously: allowing the presence of a blackbody component with temperatures in the 1000–2500 K range.

4. RESULTS

4.1. General Results

Figure 5 presents the fitting results to the SEDs of the 36 sources found in Table 2.

The 2pC model with the lowest χ^2 is shown with a long-dashed line. No additional components were added to these models.

The CLUMPY model with the highest probability is shown in Figure 5 using a thick short-dashed line which includes the sum of any additional component, if present. The additional component (blackbody or power law) is separately shown using a thick dash-dotted line.

In most cases, the probability distribution of the remaining CLUMPY models tends to be highly peaked, in the sense that the probabilities rapidly fall to values much lower than that of the best-fit model. We have divided the probability distribution into three ranges: top 50%, 50%–10%, and 10%–1% of the best-fit probability. The number of models found in each of these ranges is shown on the top-right corner of in each panel in Figure 5. At most 20 models are shown in dark-gray, medium-gray, and light-gray thin-continuous lines, for each of the probability ranges. If more than 20 models are available for each range, then only
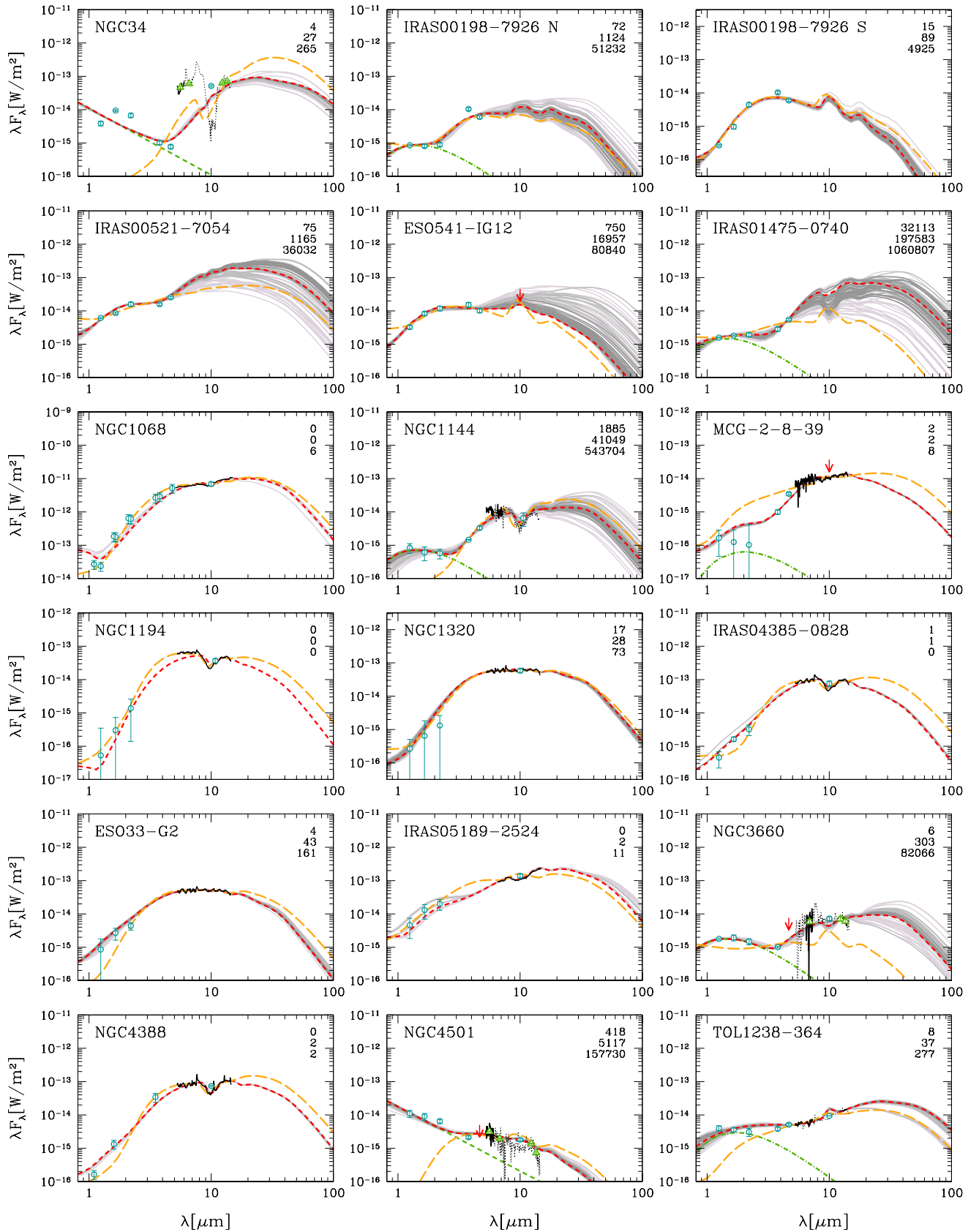
Figure 5. SED model fits determined for our sample. Photometric points are shown with circles and upper limits with arrows. Mid-IR spectroscopic observations are shown with a thin black line for those data ranges used during the fitting and with a thin dashed black line for ranges that were masked out. When the spectroscopic observations were instead binned into "photometric" points, these are shown with triangles. The best-fit 2pC model is shown with a thick long-dashed line. The best-fit CLUMPY model is shown with a thick dashed line. Up to 20 CLUMPY models in the top 50%, 50%–10%, and 10%–1% from the best-fit probability value are shown using dark-gray, medium-gray, and light-gray thin-continuous lines (see the text for further details). The number of actual models in each of these probability ranges is shown in the top-right corner of each panel.

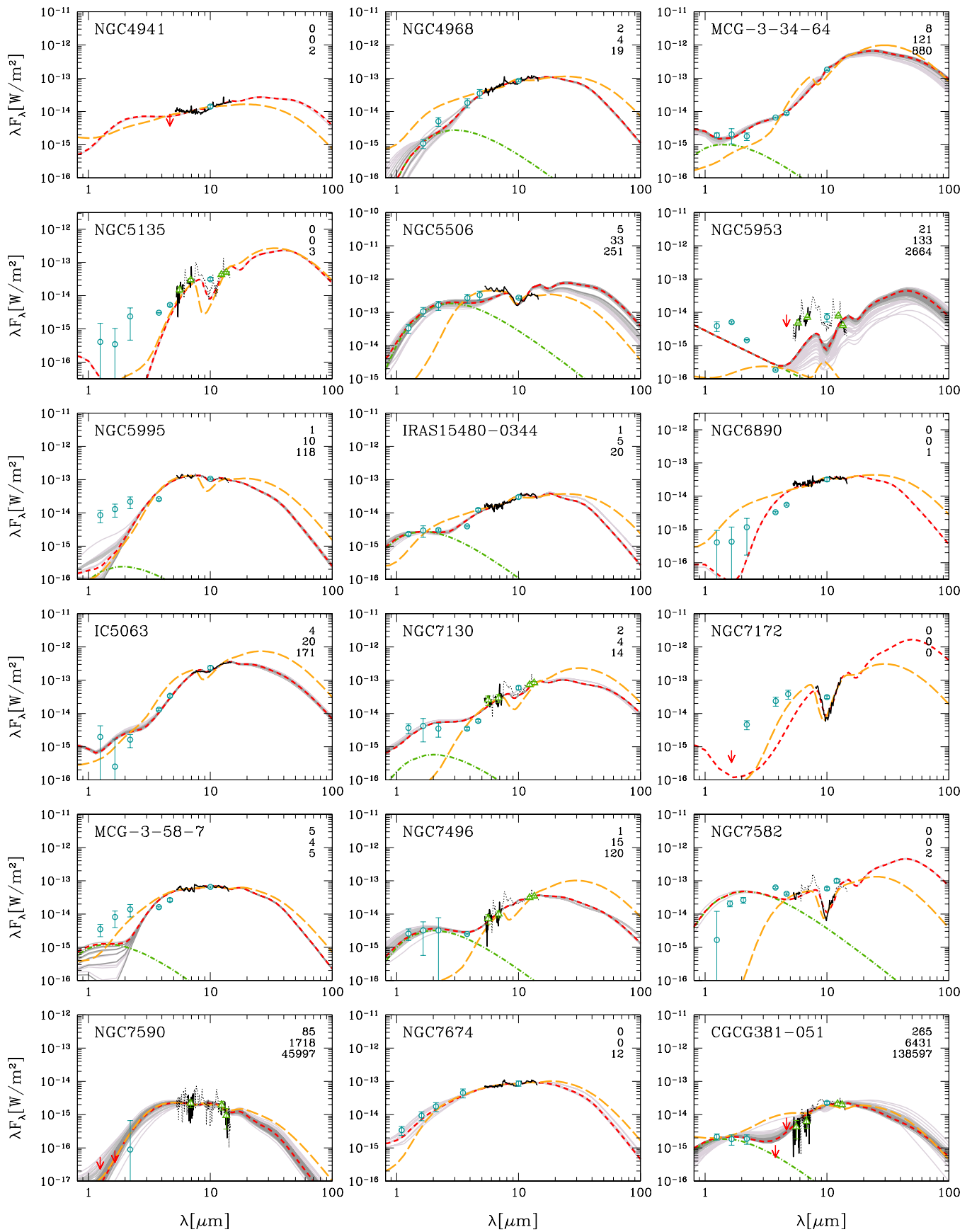(A color version of this figure is available in the online journal.)

Figure 5. (Continued)

20 models are randomly drawn from the pool of models available and shown. This gives a representation of the level of departure of the model SEDs from the best fit.

In what follows we discuss poor or inadequate fits. The previously-mentioned sources will not be considered when drawing conclusions from the fitting process in Section 4.2.

The need for mid-IR data to properly constrain the peak of the infrared emission is clearly seen in the fits to IRAS 00521−7054, ESO 541-IG12, and IRAS 01475−0740, where the best models only follow the rapid raise in near-IR flux but then flare-out for $\lambda > 10\,\mu$m due to the lack of restriction in this range. These fits are also characterized by a much less peaked model probability distribution, as shown by the large number of models in the probability ranges defined above. Therefore, all sources without mid-IR observations (this also includes IRAS 00198−7926 N and IRAS 00198−7926 S) will be excluded from the subsequent analysis. Of these discarded sources, two have $\alpha < 1$ (see Section 3.3.3).

NGC 34 and NGC 5953 show peculiar SEDs because of contamination from a starburst component, showing very strong near-IR emission. Both sources are also characterized by *Spitzer* spectra showing the largest PAH residuals seen in the sample. We used a power law to account for this component during the fitting process, but the results are poor. These two galaxies will not be considered in the analysis carried out below.

NGC 4941 lacks enough data to constrain its SED and will not be analyzed any further.

NGC 4501 presents a very steep SED throughout the near- and mid-IR, possibly because of the presence of a beamed Synchrotron jet, as already discussed. This is in sharp contrast with the SED determined by Kishimoto et al. (2009b) using the Keck interferometer, which presents a canonical shape, rising from the near-IR to the mid-IR. In our observations, the presence of a dominant power-law component means that the torus properties cannot be successfully recovered from the fitting.

In all, 27 sources will be considered in the following sections, unless otherwise noted. Of these, 14 required an extra component to account for the near-IR excess, i.e., very close to a 50% of the sample. More details are reported in Section 4.4.

4.2. Results from SED Fitting and Best-fit Parameters

4.2.1. CLUMPY Fitting Results

Table 3 presents the main results from the CLUMPY SED fitting procedure to the nuclear data of 27 sources, listing the weighted mean, the median, the mode and the 67% confidence limits for the probability distribution of each torus parameter.

Figure 6 presents the distributions of the median (in solid), average, and mode (both in dashed) parameters for the sample. Parameters are $q, \mathcal{N}_0, \sigma, \tau, \angle i, Y, A_v$ (along the line of sight), and blackbody temperature when needed. In what follows we discuss the inferred values for each parameter.

The exponent to the radial distribution of clouds shows a preference for $q \sim 0$. This corresponds to a flat distribution with the number of clouds showing a very weak dependence with the distance to the central black hole (Nenkova et al. 2008b). However, about half of the sources require larger q values.

The number of clouds along the equator shows a strongly rising distribution toward a large number of clouds, with $\mathcal{N}_0 \gtrsim 10$ being clearly favored. This was also hinted by AH11. Nenkova et al. (2008b) showed that a rather small number of clouds is required by CLUMPY models to reproduce observed SEDs, with typically $\mathcal{N}_0 \sim 5$. The difference in our findings

could be due to our sample selection, which prefers obscured, IR-bright objects. Whether IR-bright AGNs require a larger number of clouds in order to reproduce their properties is a tentative result from this work.

A large number of clouds ($\mathcal{N}_0 > 10$) push the results from the modeling of clumpy media to the limits of its parameter space (M. Elitzur 2011, private communication). This is because the current calculations compute the radiation field produced by directly illuminated clouds and then solves for those clouds found in their shadow. The emission from clouds found in the shadow of other clouds is not taken into account. A complete solution would require to iterate over the whole cloud population until a converging solution is attained. However, this is too demanding for current computer capabilities and these iterative steps are not followed (Nenkova et al. 2008a). Clearly, the larger the number of clouds, the larger the deviation between the current model prescriptions and a complete solution, particularly for compact geometries. For $\mathcal{N}_0 \to \infty$ the emission from a continuous torus should be recovered.

The torus aperture angle shows a broad distribution with a peak at $\gtrsim 60°$ and about 70% of the sources require $\sigma > 40°$. This is in agreement with AH11 who found that this is the case for Seyfert II galaxies, while Seyfert Is might show a narrower distributions of torus aperture angles.

The optical depth of individual clouds in the V band is constrained to small values around $\tau \lesssim 30$, although some sources require larger values.

The distribution of torus viewing angles shows that some objects are well fitted using intermediate values of $\angle i$, but about half of the sample requires angles of $70°$–$90°$, reflecting the fact that our sample is IR-selected, and therefore should not be biased against heavily obscured objects.

The distribution of torus thickness, Y, shows a tendency toward small values, with the bulk of the population requiring $Y \lesssim 40$. Nenkova et al. (2008b) argued that given the level of isotropy observed in the IR emission of AGNs, torus should be rather compact ($Y \lesssim 20$) or present a steep ($q \sim 2$) rather than flat ($q \sim 0$) cloud distribution. We do not see this trend: sources with small and large values of Y all are more likely to require $q \sim 0$.

The number of clouds along the line of sight can be determined using the expression

$$\mathcal{N}(\beta) = \mathcal{N}_0 \exp(-\beta^2/\sigma^2), \qquad (2)$$

where β is the angle between the torus equator and the line of sight (i.e., $\beta = 90 - \angle i$). The product of the number of clouds and the optical depth of each cloud gives total optical depth of the torus along the line of sight in the V band:

$$A_V = 1.1\tau\mathcal{N}(\beta). \qquad (3)$$

Because of the rather narrow distribution of the values of τ and $\mathcal{N}_0$, the distribution of the total optical depth shows a strong peak at $A_V \sim 30$–300.

The temperature of the blackbody component is an additional parameter for the fits. The distribution of temperature values shows that most objects require a very high temperature ($T > 1500$ K) and only two fits require $T \sim 1200$ K.

Crucially, the addition of a secondary component does not change the torus parameter distributions. Individually, only a few sources show significant changes in some parameters after the blackbody component is added (see Table 3). This can also be seen collectively when comparing the histograms

Table 3
CLUMPY Model Results

Object	τ				Y				$\angle i$				q			
	mean	mod	med	67% CL	mean	mod	med	67% CL	mean	mod	med	67% CL	mean	mod	med	67% CL
NGC 1068 ℓ	44	30	34	22–58	20	20	20	12–22	81	80	80	75–85	0	0	0	0–0
NGC 1144 BB	34	20	28	8–38	56	30	54	8–72	66	90	71	55–95	1	1	1	0–2
NGC 1144	56	60	59	42–68	56	30	55	12–78	34	0	29	0–45	1	1	1	0–2
MCG-2-8-39 BB	114	100	112	98–122	5	5	5	2–8	37	40	40	35–45	3	3	3	2–3
MCG-2-8-39	114	100	112	98–122	56	30	56	8–72	27	20	24	15–35	3	3	3	2–3
NGC 1194	12	10	11	8–18	5	5	5	2–8	40	40	40	35–45	0	0	0	0–0
NGC 1320 ℓ	12	10	11	8–18	76	90	76	58–92	17	20	19	15–35	2	2	2	1–2
IRAS 04385−0828	20	20	20	12–22	5	5	5	2–8	0	0	0	0–5	1	1	1	0–1
ESO 33-G2	20	20	20	12–22	54	20	52	8–72	32	40	38	35–65	2	2	2	2–2
IRAS 05189−2524	108	100	108	98–132	12	10	11	8–18	18	10	11	5–15	0	0	0	0–0
NGC 3660 BB	91	60	86	58–148	48	5	48	2–68	56	90	62	35–95	2	3	3	2–3
NGC 3660	149	150	149	122–150	56	90	56	8–78	29	30	31	25–45	2	2	2	2–3
NGC 4388	20	20	20	12–22	12	10	11	8–18	3	0	2	0–5	0	0	0	0–0
TOL 1238−364 ℓ BB	150	150	150	122–150	20	20	20	12–22	71	70	70	65–75	0	0	0	0–0
TOL 1238−364	150	150	150	122–150	20	20	20	12–22	60	60	60	55–65	0	0	0	0–0
NGC 4968 ℓ BB	5	5	5	2–8	91	90	91	88–98	90	90	90	75–95	0	0	0	0–0
NGC 4968 ℓ	5	5	5	2–8	90	90	90	82–92	88	90	89	75–95	0	0	0	0–0
MCG-3-34-64 BB	150	150	150	122–150	12	10	11	8–18	83	90	85	75–95	0	0	0	0–1
MCG-3-34-64	150	150	150	122–150	14	10	12	8–18	77	80	78	55–85	0	0	0	0–1
NGC 5135 ℓ	45	30	34	22–58	50	50	50	42–52	81	80	80	75–85	0	0	0	0–0
NGC 5506 BB	52	40	48	38–62	15	10	14	8–18	14	20	16	0–25	1	1	1	0–1
NGC 5506	60	60	61	58–68	20	20	20	12–22	8	10	8	5–15	0	0	0	0–1
NGC 5995 BB	12	10	11	8–18	54	90	45	12–78	72	70	71	65–75	2	2	2	2–3
NGC 5995	12	10	11	8–18	62	90	68	32–92	86	90	87	75–95	2	2	2	2–3
IRAS 15480−0344 ℓBB	9	10	9	2–12	74	70	73	62–78	90	90	90	75–95	0	0	0	0–0
IRAS 15480−0344 ℓ	45	30	34	22–58	90	90	90	82–92	90	90	90	75–95	0	0	0	0–1
NGC 6890	5	5	5	2–8	50	50	50	42–52	90	90	90	75–95	0	0	0	0–0
IC 5063	80	80	81	78–88	23	20	20	8–22	76	80	77	55–85	3	3	3	2–3
NGC 7130 ℓ BB	150	150	150	122–150	30	30	30	22–32	90	90	90	75–95	0	0	0	0–0
NGC 7130 ℓ	150	150	150	122–150	30	30	30	22–32	80	80	80	75–85	0	0	0	0–0
NGC 7172	60	60	61	58–68	100	100	100	92–102	40	40	40	35–45	0	0	0	0–1
MCG-3-58-7 BB	5	5	5	2–8	20	20	20	12–22	90	90	90	75–95	0	0	0	0–0
MCG-3-58-7	5	5	5	2–8	20	20	20	12–22	90	90	90	75–95	0	0	0	0–0
NGC 7496 BB	150	150	150	122–150	12	10	11	2–12	7	0	5	0–15	2	2	2	2–3
NGC 7496 PL	150	150	150	122–150	10	10	10	2–12	21	20	22	15–35	2	2	2	2–3
NGC 7496	150	150	150	122–150	5	5	5	2–8	25	20	25	15–35	0	0	0	0–0
NGC 7582 BB	47	40	43	32–48	100	100	100	92–102	30	30	30	25–35	0	0	0	0–1
NGC 7582	47	40	43	32–48	100	100	100	92–102	30	30	30	25–35	0	0	0	0–1
NGC 7590	8	5	7	2–12	49	5	47	2–68	71	90	79	65–95	2	2	2	2–3
NGC 7674 ℓ	45	30	34	22–58	12	10	11	8–18	70	70	70	65–75	0	0	0	0–1
CGCG 381−051 BB	145	150	146	118–150	39	5	29	2–58	15	0	12	0–25	3	3	3	2–3
CGCG 381−051	148	150	148	112–150	47	5	44	2–68	10	0	8	0–15	3	3	3	2–3

Object	$\mathcal{N}_0$				σ (°)				$T(K)/\alpha$[a]				$\log A_V(\mathrm{los})$[b]		
	mean	mod	med	67% CL	mean	mod	med	67% CL	mean	mod	med	67% CL	mean	mod	med
NGC 1068 ℓ	4	4	4	4–4	27	30	28	22–38	...	...	...	...	2.3	2.4	2.1
NGC 1144 BB	11	15	11	6–14	49	60	51	38–68	2264	2500	2300	2150–2550	2.5	2.7	2.5
NGC 1144	10	12	11	6–14	50	60	52	38–68	...	...	...	...	2.2	2.8	2.2
MCG-2-8-39 BB	8	8	8	8–8	60	60	60	52–68	1818	1800	1803	1750–1850	2.7	2.9	2.7
MCG-2-8-39	7	7	7	6–8	60	60	60	52–68	...	...	...	...	2.4	2.7	2.4
NGC 1194	15	15	15	14–16	60	60	60	52–68	...	...	...	...	2.0	2.3	2.0
NGC 1320 ℓ	14	15	15	12–16	49	45	48	38–52	...	...	...	...	1.3	2.0	1.3
IRAS 04385−0828	15	15	15	14–16	45	45	45	38–52	...	...	...	...	0.8	1.4	0.8
ESO 33-G2	5	4	5	4–6	53	60	54	38–68	...	...	...	...	1.5	2.1	1.6
IRAS 05189−2524	6	6	6	6–6	60	60	60	52–68	...	...	...	...	2.2	2.4	2.1
NGC 3660 BB	11	10	11	6–12	48	60	54	38–68	2441	2500	2462	2350–2550	2.8	3.3	2.9
NGC 3660	14	15	14	12–15	31	30	30	22–38	...	...	...	...	1.6	2.8	1.7
NGC 4388	11	11	11	10–12	60	60	60	52–68	...	...	...	...	1.5	1.8	1.5
TOL 1238−364 ℓ BB	8	8	8	6–8	15	15	15	8–22	2042	2000	2002	1750–2150	2.4	2.9	2.4
TOL 1238−364	13	13	13	12–14	15	15	15	8–22	...	...	...	...	1.6	2.8	1.6
NGC 4968 ℓ BB	15	15	15	14–15	60	60	60	52–68	1214	1200	1203	1050–1350	1.9	2.1	1.9
NGC 4968 ℓ	15	15	15	14–15	60	60	60	52–68	...	...	...	...	1.9	2.1	1.9
MCG-3-34-64 BB	14	15	14	14–15	46	45	46	38–52	2293	2500	2336	2150–2550	3.3	3.4	3.4
MCG-3-34-64	13	14	14	12–15	49	45	48	38–52	...	...	...	...	3.3	3.4	3.3
NGC 5135 ℓ	13	13	13	12–14	60	60	60	52–68	...	...	...	...	2.8	2.9	2.7

Table 3
(Continued)

Object	$\mathcal{N}_0$				σ (°)				$T(K)/\alpha$[a]				$\log A_V(\text{los})$[b]		
	mean	mod	med	67% CL	mean	mod	med	67% CL	mean	mod	med	67% CL	mean	mod	med
NGC 5506 BB	14	15	14	12–15	60	60	60	52–68	1244	1200	1236	1150–1350	2.2	2.6	2.2
NGC 5506	15	15	15	14–15	45	45	45	38–52	. . .	. . .	. . .	. . .	1.5	2.2	1.6
NGC 5995 BB	14	14	14	14–14	59	60	60	52–68	1564	1900	1817	1050–1950	2.2	2.4	2.2
NGC 5995	12	12	12	12–12	60	60	60	52–68	. . .	. . .	. . .	. . .	2.2	2.4	2.2
IRAS 15480−0344 ⸮BB	7	5	5	4–12	15	15	15	8–22	2415	2500	2428	2350–2550	1.9	2.2	1.7
IRAS 15480−0344 ⸮	2	2	2	2–2	16	15	16	8–22	. . .	. . .	. . .	. . .	2.0	2.2	1.9
NGC 6890	15	15	15	14–16	15	15	15	8–22	. . .	. . .	. . .	. . .	1.9	2.1	1.9
IC 5063	14	13	14	12–14	60	60	60	52–68	. . .	. . .	. . .	. . .	3.0	3.1	3.1
NGC 7130 ⸮ BB	8	8	8	8–8	15	15	15	8–22	2176	2500	2191	1750–2350	3.1	3.1	3.1
NGC 7130 ⸮	11	11	11	10–12	15	15	15	8–22	. . .	. . .	. . .	. . .	3.1	3.3	3.1
NGC 7172	15	15	15	14–15	60	60	60	52–68	. . .	. . .	. . .	. . .	2.7	2.9	2.7
MCG-3-58-7 BB	15	15	15	14–15	21	15	21	8–38	2150	2000	2043	1850–2250	1.9	2.1	1.9
MCG-3-58-7	15	15	15	14–15	15	15	15	8–22	. . .	. . .	. . .	. . .	1.9	2.1	1.9
NGC 7496 BB	15	15	15	14–15	60	60	60	52–68	1865	1800	1835	1750–1950	2.5	2.9	2.5
NGC 7496 PL	14	15	15	14–16	60	60	60	52–68	0.39	0.39	0.39	0.44–0.34	2.8	3.1	2.8
NGC 7496	14	15	14	12–15	45	45	45	38–52	. . .	. . .	. . .	. . .	2.4	2.9	2.5
NGC 7582 BB	15	15	15	14–15	60	60	60	52–68	1696	1700	1698	1650–1750	2.4	2.6	2.4
NGC 7582	15	15	15	14–15	60	60	60	52–68	. . .	. . .	. . .	. . .	2.4	2.6	2.4
NGC 7590	11	13	11	8–14	40	60	42	22–68	. . .	. . .	. . .	. . .	1.9	2.3	1.9
NGC 7674 ⸮	5	5	5	4–6	15	15	15	8–22	. . .	. . .	. . .	. . .	1.6	2.3	1.5
CGCG 381−051 BB	12	13	12	10–15	53	60	54	38–68	2283	2500	2320	2150–2550	2.4	3.0	2.4
CGCG 381−051	12	15	13	10–15	35	30	33	22–38	. . .	. . .	. . .	. . .	1.0	1.7	0.7

Notes. Model results from the fitting procedure using CLUMPY models. For each parameter the average (*mean*), the mode (*mod*), and the median (*med*) with 1σ confidence limits (CL) of the probability distribution are given. Because of the discrete nature of the parameter space, for very narrow probability distributions the CLs can correspond to the same parameter value. A ⸮ indicates Compton-thick (CT) sources. Objects that were also modeled using a blackbody or power-law component are labeled using a BB or PL. [a]Temperature of the blackbody (BB) or index of the power-law (PL) secondary component. [b]The value of A_V along the line of sight are calculated following the equation found in the text. Therefore, no associated error estimates are given.
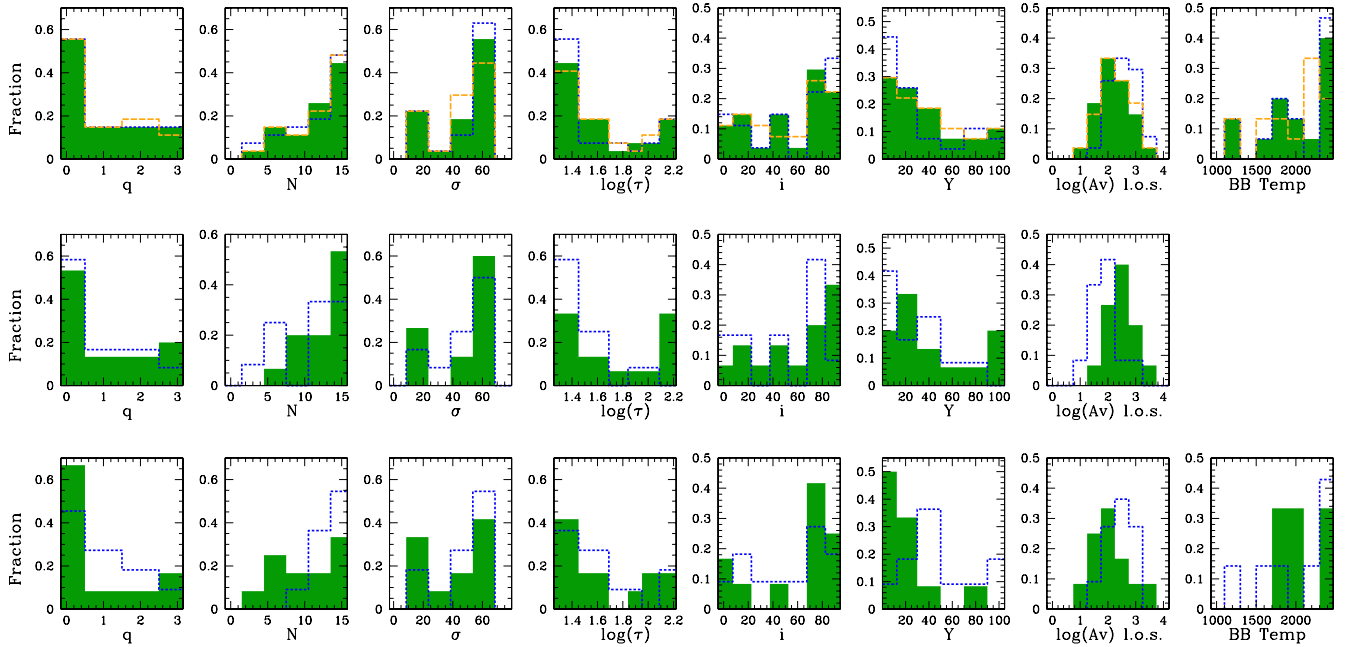

Figure 6. Top: distribution of the best-fitted values of q, $\mathcal{N}_0$, σ, τ, $\angle i$, Y, $\log A_V(\text{los})$, and temperature of the additional blackbody component if needed. The panels show the normalized histograms of the median (solid), and average and mode distributions (dashed lines) for the 26 objects with acceptable fits. Middle: median distribution for objects that require a blackbody component during their SED fitting (solid), compared with those that do not (dashed). Bottom: median distribution for objects with a detected HBLR (solid), compared with those without an HBLR (dashed).

(A color version of this figure is available in the online journal.)

for objects where an additional component was required and for those where the torus model alone yielded a good fit (middle panels in Figure 6). The distributions are almost indistinguishable.

4.3. Previous CLUMPY Fitting Results

To check how robust our results are, we compare our best-fit parameters with previous work which have studied common

Table 4
Comparison of Model Parameters from RA09, AH11, and This Work

Galaxy	RA09		AH11		This Work	
Parameter	*med*	*mod*	*med*	*mod*	*med*	*mod*
NGC 1068						
q	...	...	2.2	2.0	0	0
$\mathcal{N}_0$	...	...	14	15	4	4
σ	...	...	26	21	30	28
τ	...	...	49	49	30	34
$\angle i$	...	...	88	89	80	81
IC 5063						
q	<1.5	0.4	2.6	0.8	3	3
$\mathcal{N}_0$	>11	14	14	15	14	13
σ	>57	75	60	47	60	60
τ	70	66	130	99	81	80
$\angle i$	>65	89	82	84	82	90
NGC 5506						
q	2.5	2.7	0.4	0.3	0.7	1
$\mathcal{N}_0$	<2	1	14	15	14	15
σ	25	15	43	40	60	60
τ	<68	22	100	99	48	40
$\angle i$	85	85	34	35	16	20
NGC 7172						
q	>1.7	2.9	1.1	1.5	0.5	0.5
$\mathcal{N}_0$	5	5	13	15	15	15
σ	>54	74	61	68	60	60
τ	<12	10	59	52	60	61
$\angle i$	>45	89	77	85	50	50
NGC 7582						
q	>2.5	3.0	0.3	0.1	0.5	0.5
$\mathcal{N}_0$	<2	1	13	15	15	15
σ	<29	16	48	49	60	60
τ	<27	14	89	97	40	43
$\angle i$	41	58	12	0	30	30

Notes. RA09 and AH11 limited the range of Y to values up to 30. AH11 also incorporated a foreground host absorption component during their fitting corresponding to $A_V = 7, 11$, and 8–13 mag for IC 5063, NGC 5506, and NGC 7582, respectively.

Table 5
2pC Model Results

Object	$\tau_{9.7}$	p	q	i	χ^2
NGC 1068 ≀	20	0	4	50	4
NGC 1144	20	1	4	80	3
MCG-2-8-39	20	0	0	40	44
NGC 1194	5	1	4	90	4
NGC 1320 ≀	10	1	6	70	3
IRAS 04385−0828	10	0	6	80	7
ESO 33-G2	10	1	4	50	3
IRAS 05189−2524	20	0	4	40	0.1
NGC 3660	0.1	0	6	0	30
NGC 4388	5	0	2	70	8
TOL 1238−364	20	0	0	40	11
NGC 4968 ≀	15	0	0	40	14
MCG-3-34-64	20	0	0	50	44
NGC 5135 ≀	20	0	0	80	82
NGC 5506	5	1	4	90	7
NGC 5995	10	1	6	80	5
IRAS 15480−0344 ≀	20	0	0	40	13
NGC 6890	15	0	0	40	23
IC 5063	10	0	0	50	24
NGC 7130 ≀	20	0	0	60	45
NGC 7172	10	0	0	90	53
MCG-3-58-7	15	1	6	60	6
NGC 7496	20	0	0	50	460
NGC 7582	5	0	0	80	25
NGC 7590	5	1	6	80	9
NGC 7674 ≀	20	1	4	50	3
CGCG 381−051	20	0	2	0	5

Note. Model results from the fitting procedure using 2pC two-phase models. As before, a ≀ indicates Compton-thick (CT) sources.

observations. Hence the SEDs are not significantly modified by the different spectral data.

Table 4 presents the median and mode of the parameter distributions determined by RA09 and AH11 and by this work for those objects common to the samples. Our approach gives very similar results to those found by AH11. The only significantly different model parameters are q and $\mathcal{N}_0$ for NGC 1068. It can be seen that the largest differences are found between the work of RA09 and AH11, due to the inclusion of spectroscopic information around $10\,\mu$m. This is a clear indication of the importance of including detailed information of the SED around the silicate absorption feature.

4.3.1. 2pC Fitting Results

Table 5 presents the results from the fitting using the 2pC models for the 27 considered sources. The χ^2 value from the best fit is also shown. About half of the sources have $\chi^2 < 10$ and we label these as acceptable fits.

By examining Figure 5, it becomes apparent that the 2pC models mostly fail to reproduce those SEDs that already represented a challenge for the CLUMPY models, namely, those with a near-IR excess and those with a strong silicate absorption accompanied by substantial near-IR emission. We have not attempted to obtain new fits using the current library of 2pC models adding a blackbody component because of the rather limited range of parameter values available when compared with the CLUMPY models.

Two parameters can be directly compared between the results obtained using 2pC and CLUMPY models: the total optical depth at the equator of the torus and the inclination angle
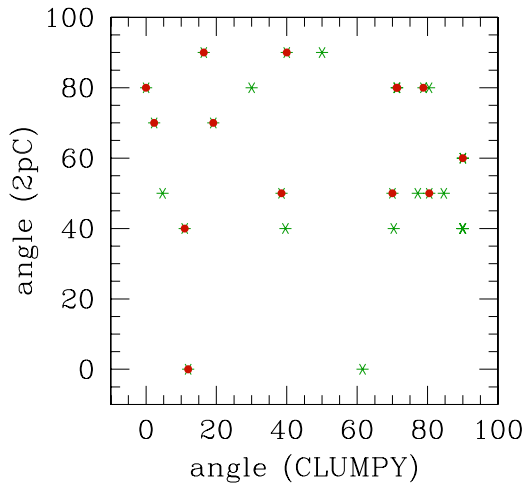
sources and which have also used the Nenkova et al. (2008a) CLUMPY models to represent the infrared SEDs of nearby AGNs. RA09 and AH11 presented the modeling of Type I, Type II, and intermediate-type Seyfert galaxies, of which five objects are in common with our sample. AH11 add N-band ground-based spectroscopy to the SEDs, while RA09 use only photometric data. They both use a Bayesian inference algorithm (Bayesclumpy; Asensio Ramos & Ramos Almeida 2009) to determine the best-fit values to a given SED and the probabilistic distribution of the inferred model parameters. Note also that AH11 limited the range of Y to values up to 30 for all objects, while the viewing angle was restricted to 30–50 for NGC 5506 and 60–90 for NGC 1068, while our only restriction was the $L_{\rm O III}^{\rm bol}$ prior described in Section 3.3.2.

For three of the objects presented by RA09 and AH11, NGC 1068, NGC 5506, and NGC 7172, the photometric measurements are common with this work (except for the Q-band measurements reported by RA09). IC 5063 and NGC 7582, on the other hand, have independent photometric observations. The ground-based spectra presented by AH11 were obtained with much higher spatial resolution than the *Spitzer* and *ISO* data used here. However, examination of the spectra shows that the ground-base data are comparable to the space-borne

Figure 7. Comparison between inclination angles obtained using the CLUMPY and 2pC models. All 27 sources are plotted with an asterisk. Sources with 2pC fits with values of $\chi^2 < 10$ are also shown with a circle.

(A color version of this figure is available in the online journal.)

subtended by the observer. Neither of these comparisons yield a proper correlation. In fact, 2pC covers an optical depth range of $\tau_{9.7} = 0.1$–20, while CLUMPY considers values has high as $\tau_{9.7} \gtrsim 100$.

Figure 7 presents the comparison between the best-fit inclinations angles. Even if only acceptable 2pC fits are taken into account, the distribution resembles a scatter plot. Again, note that 2pC models do not cover intermediate angles (smaller than $40°$ but larger than $0°$) and the opening angle of the cloud distribution is fixed to $50°$.

Therefore, it seems that the most important drawback from the 2pC models is the narrow range of parameters so far explored.

4.4. Sources with Near-IR Excess and Strong Si Absorption

As already discussed, several sources were identified in Paper I as having a near-IR upturn (i.e., $\alpha < 1$; see also Table 2) and their SEDs were fitted using an additional blackbody component, which considerably improved the quality of the fits. The required temperatures are generally very high ($T \sim$ 1700–2500 K) and the emission typically peaks at around $2 \,\mu$m. Only two sources require lower temperatures ($T \sim$ 1200 K): NGC 4968 and NGC 5506.

Several other works have found it necessary to use an additional component to explain the excess of near-IR emission observed in luminous Type I QSOs with respect to the CLUMPY torus models (Mor et al. 2009; Mor & Trakhtenbrot 2011; Deo et al. 2011; Landt et al. 2011). All these works find that the blackbody emission is characterized by $T \sim$ 1200–1400 K, while we find that the required temperatures are much higher, with $T \sim$ 1700–2500 K. These values are too high to interpret this component as emission from hot dust and therefore its nature remains unexplained. Note, however, that given the difficulties in isolating the AGN near-IR emission in obscured Seyferts compared with the dominant AGN emission in luminous QSOs might contribute to the problem.

Of the 12 sources with $\alpha < 1$ in Table 2, 3 correspond to radio-loud sources and were also fit with an additional power-law component (Section 3.3.4). IRAS 01475−0740, however, did not have enough mid-IR information to properly restrict the fitting. NGC 4501 seems to be dominated by a power law and the inclusion of this additional component allows for a proper fit to

the SED, as seen in Figure 5. This component, however, heavily dilutes the torus emission, and it is not clear whether the derived parameters are representative of its intrinsic emission. The last radio-loud source, NGC 7496, can be successfully fit using a blackbody or a power law as secondary component. Figure 5 shows the results from the fitting using a blackbody component, while Table 3 shows the best-fit parameters for both cases. It can be seen that the results are consistent with each other.

In Section 3.3.5, it was also discussed that sources presenting deep silicate absorption were fitted using an additional black-body component to supply the near-IR flux lacking in CLUMPY torus models that have a strong $9.7 \,\mu$m absorption features, which is the case of NGC 5506, NGC 7582, and NGC 7172.

A good fit was obtained for NGC 5506 and NGC 7582, as can be seen in Figure 5. In Table 3, we report results for fits with and without the blackbody component. For NGC 7172, on the other hand, no possible combination would reproduce both the extremely deep $9.7 \,\mu$m absorption feature and the near-IR photometry. However, the best-fit 2pC model provides a reasonable fit for this source. It corresponds to a model with a $90°$ inclination angle and a large $\tau_{9.7}$ value. Large $\tau_{9.7}$ corresponds in fact the regime where the two-phase medium introduces the largest departure from the clumps-only models. The CLUMPY results are also consistent with a large optical depth and high inclination angles.

Figure 5 shows that other sources require additional near-IR flux besides those with a index $\alpha < 1$ or strong Si absorption: NGC 4968, NGC 5995, and MCG-3-58-7. A very good fit was found for NGC 4968 with a CLUMPY model and a blackbody component with a temperature of $\sim$1200 K. The fits to MCG-3-34-64 and MCG-3-58-7 are rather poor in the near-IR region, but the fit provided by the 2pC models to MCG-3-58-7 is quite good ($\chi^2 = 6$). Table 3 presents the results using CLUMPY models with and without the additional blackbody component for all these sources.

It is very encouraging that the inclusion of a blackbody component does not have a significant impact on the torus parameters derived from the fitting process using CLUMPY models. This can be seen in the middle panel of Figure 6, but also when examining individual fits reported in Table 3. This is in contrast with the work of Deo et al. (2011), who found significant changes in the best-fit parameters when introducing a blackbody component to their fits. This could be due to the Type I nature of their sources and therefore a different level of constraining coming from the $9.7 \,\mu$m silicate feature in their sample of QSOs. The largest changes are seen in parameters q and Y. One of the most interesting findings from this work is that most QSOs require large inclination angles and a small number of clouds.

In summary, to solve for the lack of sufficient near-IR emission in CLUMPY torus models, we added an additional blackbody component to $\sim$50% (14/27) of our sources and obtain acceptable fits in most cases. However, the temperatures of these components are too high to correspond to dust emission, and therefore its true nature is unclear. 2pC models can provide better results for some of these sources, but the limited parameter space currently explored by these models does not allow to ascertain that the two-phase approach is a definite solution to the lack of near-IR emission in observed SEDs.

5. ANALYSIS

In the previous section, it has been established that the results obtained using CLUMPY models are quite robust to the addition

of a blackbody component in the near-IR. Because of the large parameter space explored by these models and the well-restricted results obtained for most parameters in Section 4.2.1, in what follows we will only consider CLUMPY results for our analysis.

We have compiled ancillary data for our sample from the literature. Table 2 presents results on the detection of HBLRs, [O III] fluxes and luminosities, hydrogen column densities determined from X-ray observations and hard (2–10 keV) fluxes, radio fluxes, and Balmer decrements as determined in Paper I.

5.1. The Inferred Hydrogen Columns

One of the most powerful diagnostics to characterize the different classes of AGN is the inferred hydrogen column density, N_H, as determined from the photoelectric cutoff experimented by the power-law X-ray spectrum emitted by the central source. The observed values of N_H probes the amount of material along the line of sight toward the active nuclei and correlate strongly with other diagnostics to determine the Seyfert type. In fact, it has been shown that while Type I objects suffer from little absorption, Type II systems usually present absorbing columns of 10^{22} cm^{-2} or more (Smith & Done 1996; Turner et al. 1997; Maiolino et al. 1998; Bassani et al. 1999).

However, measurements of the column N_H toward the central region obtained through other methods, such as the ratio Hα/Hβ for broad emission lines (since narrow lines would probe the extinction affecting the much more extended narrow emission line region), typically give smaller values of N_H than those obtained from X-ray observations (Maccacaro et al. 1982; Reichert et al. 1985). The optical depth can also be inferred using key features in the extinction curve, such as the 2200 Å "bump" and the silicate absorption features in the mid-IR.

Possible solutions for these differences have been postulated: a dust-free inner region (interior to the torus) could be responsible for the excess column probed by X-rays; an anomalous Hα/Hβ ratio could be due to the collisional effects present in the high-density clouds found in the BLR; the line of sight probed by the X-rays could be significantly different to that probed by other estimators; Maiolino et al. (2001a, 2001b) and Gaskell et al. (2004) argue that AGN environments might have a different dust size distribution, either because of the presence of larger grains or because small grains are depleted, although other works argue for normal dust properties in AGNs (Mason et al. 2004; Nenkova et al. 2008b). X-ray absorption by dust-free material within the sublimation radius of the torus should not be significant as this ionized gas would produce very intense narrow emission lines which are not observed (Maiolino et al. 2001a).

Shi et al. (2006) have shown that there is a broad but clear correlation between the strength of the 9.7 μm silicate feature and the N_H columns derived from X-ray data. In very broad terms, unabsorbed systems show 9.7 μm feature in emission while absorbed systems show it in absorption. In Figure 8, we compare the column density N_H along the line of sight derived from our SED fitting with those obtained from the photoelectric cutoff from X-ray observations. Arrows show objects for which $N_H > 10^{24}$–10^{25} cm^{-2} upper limits have been determined. One system has an $N_H > 10^{22}$ cm^{-2} upper limit coming from observations in the soft X-rays. No clear trend is found in the plot, and we are not able to reproduce the findings of Shi et al. (2006). Crucially, we do not find a systematic offset between the two measurements. We also show the combination of parameters $\mathcal{N}_0$ and τ to yield the total Hydrogen column N_H (assuming a
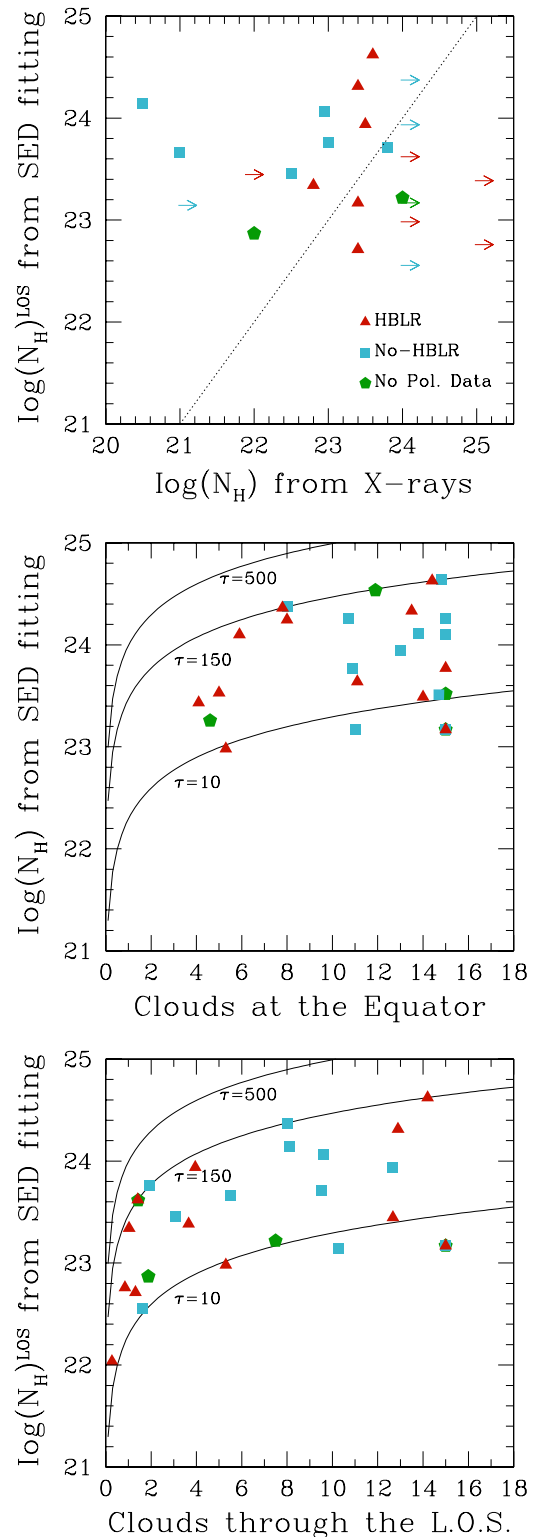

Figure 8. Top panel: comparison of column densities along the line of sight, N_H (cm^{-2}), derived from the CLUMPY emission models for the torus and derived through X-ray observations. Middle panel: distribution of the number of clouds at the torus equator ($\mathcal{N}_0$) vs. the total N_H column derived from our fittings, also at the equator. Continuous lines correspond to the total opacity for different optical depths of individual clouds ($\tau = 10, 150, 500$). Bottom panel: the same as above but this time showing the number of clouds ($\mathcal{N}(\beta)$) and the N_H column along the line of sight.

(A color version of this figure is available in the online journal.)

gas-to-dust ratio $N_H/A_v = 1.79 \times 10^{21}$ cm^{-2} mag^{-1}) at the torus equator and along the line of sight.

The presence of clumpy media around the active nucleus seems to be the best way to interpret our results. While our SEDs probe the average conditions of the dusty medium *in emission*, the X-rays probe a particular line of sight toward the nucleus *in absorption*. Rapid and dramatic changes of the X-ray N_H in NGC 1365 and NGC 4388 (Risaliti et al. 2005; Elvis et al. 2004) seem to validate this scenario (although Elvis et al. oppose it).

So, can we consider our column densities to be more representative of the average, long-term conditions of the physical conditions of the duty torus? Probably yes, but these will have to be revised as new models and better observations come along in the future. Since from the model fitting no N_H values are found outside the $10^{22.5}$–10^{25} cm^{-2}, this might be a reasonable range of columns to be adopted as representative of the average values for Type II Seyferts.

Compton-thick nuclei are defined as those where the X-ray derived N_H columns are in excess of 10^{24}–10^{25} cm^{-2}. The current compilation of N_H columns presented in Table 2 shows that of the total number of objects with measured column densities (30 out of the 39 galaxies in the full sample), 11 are Compton thick. This is in line with previous findings (Risaliti et al. 1999; Bassani et al. 1999, 2006).

Out of the 11 CT sources found in our sample, 8 have acceptable SED fits: the bona fide CT galaxy NGC 1068, NGC 1320, TOL 1238−364, NGC 4968, NGC 5135, F 15480−0344, NGC 7130, and NGC 7674. The inferred angle that the torus axis subtends with our line of sight is in the 70°–90° range for seven objects, while for NGC 1320 the angle found is rather small (∼20). See Table 3.

AH11 have shown that the probability for photons to escape the obscuring material can still be low for systems with intermediate inclinations, provided that the angle subtended by the torus is fairly large. This is the case for most of our Seyfert II systems that present rather large values of σ. The exceptions are TOL 1238−364, IRAS 15480−0344, NGC 6890, NGC 7130, MCG-3-58-7, and NGC 7674. Interestingly, four of these sources are CT systems. It should be remembered, however, that the X-ray derived N_H columns measure a very specific line-of-sight property of the central region, as clearly validated by those objects with variable columns (Risaliti et al. 2005; Elvis et al. 2004).

Elitzur (2012) has recently proposed that Type I and Type II nuclei are examples of objects preferentially drawn from the two ends of the distribution of torus covering factor, with Type II sources being examples of particularly puffed-up tori, characterized by large values of $\mathcal{N}_0$ and σ. This is clearly supported by our results.

5.2. The Presence of Hidden Broad-line Regions

The presence of an HBLR is the most clear indication that at least some Type II AGNs have broad emission lines. About 40% of the Seyfert 2 galaxies in the 12 μm Sample are found to have HBLRs, in agreement with the fraction found in optically selected Seyfert 2 samples (Tran 2003). The fraction is closer to 50% for the 27 objects with good SED fittings. Unfortunately, there are significant differences in the sensitivity of the spectropolarimetric studies found in the literature and since the data are not provided in many of these works it is not possible to visually verify the presence or absence of the HBLRs.

The reasons behind the lack of detection of an HBLR in some Type II sources have been a matter of heated debate (Heisler et al. 1997; Alexander 2001; Gu et al. 2001; Tran 2001, 2003; Lumsden & Alexander 2001; Deluit 2004; Lumsden et al. 2004; Zhang & Wang 2006; Shi et al. 2006; Haas et al. 2007). Some works advocate that the non-detection of an HBLR is due to the presence of a dominant galaxy component that dilutes the emission from the active nucleus. Others interpret the observations as evidence for the existence of a different class of AGNs where a BLR is not present.

It could be imagined that in objects that truly lack a BLR, no dusty structure needs to be present either, but this does not have to be the case. The non-HBLR objects might have an active nucleus *and* a torus, lacking only the BLR. Evidence seems to support this: Haas et al. (2007) looked at the mid-IR properties of a sample of Seyfert galaxies as obtained with high spatial resolution images and found that the nuclear properties of the 12 μm/[O III] ratio showed no distinction between sources with or without an HBLR. This seems to suggest that despite the presence or absence of the HBLR, hot dust is still present in the nuclear region of both types of sources.

Besides, Tran (2003) finds that although the IRAS 25 μm/60 μm color and the luminosity of the AGN are well correlated with the presence of an HBLR, the level of extinction toward the nuclei is similar in both types of sources.

We find some indications that sources with and without an HBLR might have systematic differences in their infrared emission. Bottom panels in Figure 6 suggest that for sources with an HBLR the torus might be less extended than for sources with an undetected HBLR. However, as already discussed in Section 5.2, the parameter Y is not well constrained by the fitting process of our data.

Sources with an HBLR also might have systematically smaller line-of-sight extinction values than sources with an undetected HBLR. Equation (2) states that the number of clouds along the line of sight depends on the number of equatorial clouds ($\mathcal{N}_0$), the thickness of the torus (σ), and the inclination angle ($\angle i$). Figure 6 shows that σ is very similar for sources with and without an HBLR, while $\angle i$ does not show a statistically significant difference. The number of clouds, on the other hand, presents clearer differences between sources with and without an HBLR. This can also be seen in Figure 8 where nuclei with an HBLR cover a wide range of number of clouds at the torus equator, while nuclei without an HBLR cluster at the higher end of the distribution. However, Figure 8 also shows that these differences are much less clear when looking at the number of clouds along the line of sight, $\mathcal{N}(\beta)$, a parameter much closely related to the line-of-sight A_V (Equation (3)). Kolmogorov–Smirnov (KS) tests in fact do not confirm that the perceived differences are statistically significant.

If further evidence that the different distributions of the line-of-sight A_V for sources with and without an HBLR are different is found, we need to explore some possible explanations. At face value this contradicts a strict unification scheme, where the only difference between Type I and Type II sources is the view point of the observer. However, is becoming clear that a strict unification scheme is not plausible (Elitzur 2012).

We can postulate that a larger number of clouds obscure the polarized emission from the BLR. This would require a rather compact scattering region, with a comparable scale height as that of the torus itself. This result is in agreement with the analysis presented in Lumsden et al. (2004) where it is claimed that the fraction of Seyfert galaxies with an HBLR is larger when

looking at only Compton-thin nuclei (as determined by X-ray observations), implying a sample of sources with less obscured central regions.

5.3. Torus Sizes and Masses

The CLUMPY modeling does not provide an absolute torus size, but instead the parameter $Y = R_{out}/R_{in}$. While most of the fits favor $Y < 50$, some sources can have a very extended torus with $Y \lesssim 100$ (see Figure 6).

Clumpy torus models are characterized by clouds showing a range of temperatures for a given distance from the central source (Nenkova et al. 2008b; Schartmann et al. 2005). This is in sharp contrast with the predictions from a continuous dust distributions, where a unique temperature is found as a function of radius. Hence, the SED shapes for CLUMPY models are not very sensitive to the Y parameter or the size of the torus. Nenkova et al. (2008b) show that observations below 5 μm will not be able to distinguish between Y values, irrespective of the cloud distribution, which is determined by the q parameter. At longer wavelengths, some differences can be appreciated for a flat cloud distribution ($q \sim 1$), but these are only significant for wavelengths above 15 μm and therefore are not well probed by our observational SEDs (see also Section 5.5).

Following the results from Suganuma et al. (2006), we can assume that R_{in} is indeed set by the dust sublimation radius as $R_{in} = 0.4\sqrt{(L^{bol}/10^{45})}$ pc, where L^{bol} is in units of erg s^{-1}. As already explained, we have used the [O III] luminosities listed in Table 2 as a prior for the intrinsic nuclear luminosities in our sources and found that the torus inner radii vary between 0.05 and 1 pc.

Torus outer sizes (R_{out}) are presented in Figure 9. As can be seen, there is a wide distribution of R_{out}, but most of them are below 5 pc in extent, with some torus being as small as 0.1 pc.

The total mass of the torus can be estimated as (Nenkova et al. 2008a)

$$M_{torus} = 4\pi m_H \sin(\sigma) N_H^{eq} R_{in}^2 Y I_q(Y), \quad (4)$$

where N_H^{eq} is the equatorial column density of the torus, R_{in} is calculated as the dust sublimation radius, σ and Y are parameters of the model, and I_q is 1 if $q = 2$ or 3, $Y/2 \ln Y$ if $q = 1$, or $Y/3$ if $q = 0$. We find some torus masses, up to $10^7 M_\odot$, as shown in Figure 9. However, in most cases these are driven by large Y values, a parameter not well constrained by the best-fitting results. Still, Siebenmorgen et al. (2005) reported the dust masses implied by a simple model of the dust emission in two quasars, being of the order of 10^6–$10^7 M_\odot$. Fritz et al. (2006) reported on the masses implied by the smooth modeling of the emission of Type I and Type II Seyferts, ranging from ~ 70 to $10^7 M_\odot$. Our results show a strong peak, however, with most masses in the $\gtrsim 10^4 M_\odot$ range, as also seen by AH11.

5.4. Comparison with Interferometric Observations

Infrared interferometric observations are providing the ultimate way to observe the putative dusty torus in AGNs. Unfortunately, this technique is limited to the brightest sources and the observations required are very expensive and difficult to obtain.

Until now, long-based interferometry has been carried out for a couple of dozen Type I and Type II AGNs (Wittkowski et al. 1998, 2004; Weinberger et al. 1999; Swain et al. 2003; Weigelt et al. 2004; Jaffe et al. 2004; Meisenheimer et al. 2007; Tristram et al. 2007; Beckert et al. 2008; Kishimoto et al. 2009a, 2009b; Raban et al. 2009), with the largest sample found in Tristram
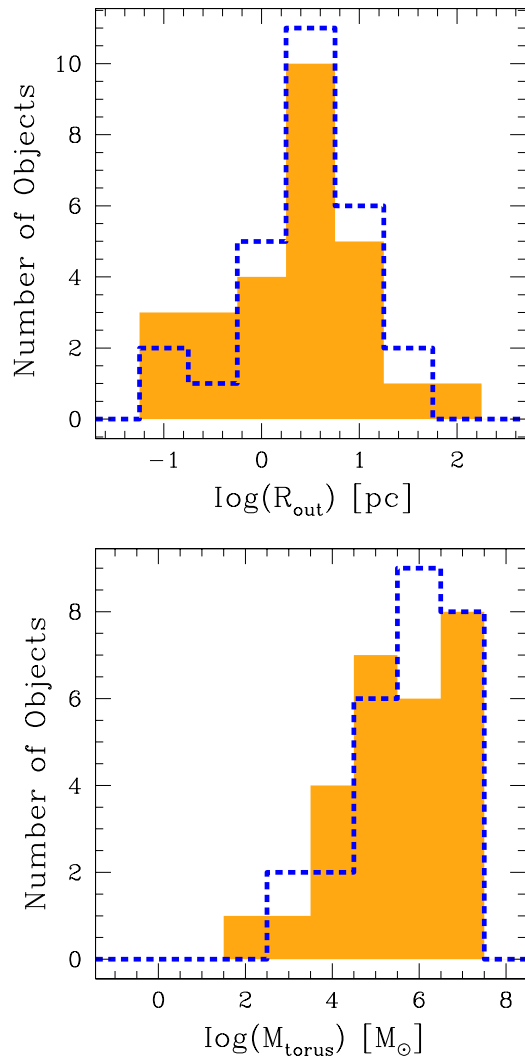

Figure 9. Distribution of torus outer radii (R_{out}) and masses (M). The median distribution is shown in the solid color, while the mode distribution is shown with a dashed line.

(A color version of this figure is available in the online journal.)

et al. (2009). Four objects in this last work are in common with our sample, NGC 1068, F 05189−2524, NGC 5506, and NGC 7582; however, the observations for NGC 5506 and NGC 7582 did not provide useful data, while for F 05189−2524 only a very faint fringe detection was possible. Also, it has been realized that interferometric studies yield more unambiguous results in Type I sources (see the discussion in Kishimoto et al. 2011). Therefore, a one-to-one target comparison is not possible.

However, for most of those sources where interferometric observations have provided restricting results, the sizes of the resolved structures observed in the near- and mid-IR are of the order of a few parsecs (see references above). These are already in good agreement with the results from the dust reverberation determined by Suganuma et al. (2006), where the inner face of the torus is found at the dust sublimation radius which directly depends on the luminosity of the central source, and with the results derived in this work.

5.5. Radio Loudness

Ho (1999) was the first to note that radio loudness is a function of the AGN bolometric luminosity, with low-luminosity objects
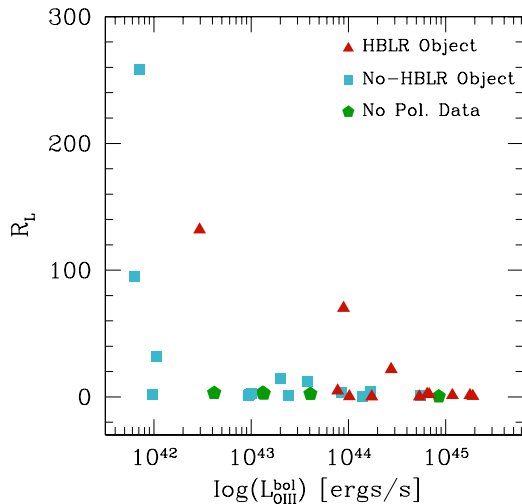
Figure 10. Radio loudness, as defined by the parameter R_L vs. bolometric luminosity. The presence of an HBLR is also indicated.

(A color version of this figure is available in the online journal.)

Figure 11. Luminosity of the 6.2 μm PAH feature, as a tracer of star-forming activity, vs. total obscuration at the equator of the modeled torus. The symbols are the same as in Figure 10.

(A color version of this figure is available in the online journal.)

(those below $\sim 10^{43}$ erg s^{-1}) being more likely to have a radio-loud central source. We can see this trend in Figure 10, which includes all sources with L^{bol} and R_L measurements. It can be seen that the probability of being radio loud increases with L^{bol}.

It is interesting to see that for those radio-loud sources with acceptable fits (F 04385−0828 and NGC 7496) a very small inclination angle to the line of sight is derived from the SED results. This is in line with an orientation effect to be responsible for the boosting of the radio emission, although theoretical predictions state that the scaling between the radio and the optical output should depend weakly on the relativistic Doppler factor (Falcke et al. 2004). Further data would be needed to confirm this finding.

In Figure 10, we also include information about objects with HBLR detections. There seems to be a trend for more luminous nuclei to show the presence of polarized BLRs as already noticed by other works and in line with the hypothesis that weaker nuclear sources are outshined by the stellar components (see references in Section 5.2).

5.6. Correlation with Star Formation

One important subject to discuss is whether the presence of nuclear obscuration is related to the level of star formation in the nucleus vicinity. Taken at face value, this scenario opposes the Unified Model, since in principle the only difference between a Type I and a Type II source is the viewing angle. However, this is true only if all tori are exactly the same.

As already discussed, Elitzur (2012) has recently proposed that Type II objects are examples of particularly puffed-up tori, with larger $\mathcal{N}_0$ and σ values. In turn this could result in a larger mass of cold dust, because of larger shadowing from the central source which allows for dust to cool more efficiently at large radii.

In Paper I, we have used diagnostic diagrams to determine the presence of star formation in the nuclear region. Essentially, there is no correlation between the level of star formation and the parameters that control the thickness of the torus, $\mathcal{N}_0$ and σ.

We can also look at the more extended star formation using the observed luminosity of the 6.2 μm PAH feature. No evidence for such correlation is found between the strength of the PAH
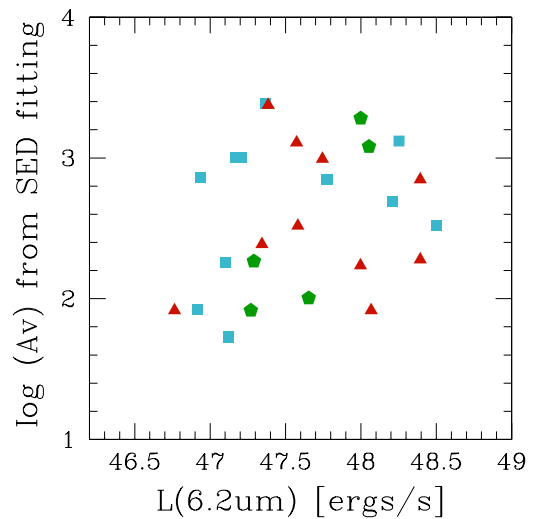
feature and the amount of extinction determined from the SED fitting, as can be seen in Figure 11.

6. SUMMARY AND CONCLUSIONS

We have performed the fitting of the near- and mid-IR SEDs of a sample of 36 Seyfert II galaxies using CLUMPY and 2pC models developed by Nenkova et al. (2002, 2008a, 2008b, 2010) and Stalevski et al. (2012). Adequate fits were reported for 27 sources.

Our conclusions are the following.

1. Observations in the mid-IR, and in particular N-band spectroscopy of the sources, are crucial to perform an adequate fitting to the SEDs.
2. The use of the bolometric luminosity of the source as a prior during the fitting is also an important tool to constrain the best-fit results.
3. We find that the best-fit parameters for the CLUMPY models correspond to $\mathcal{N}_0 \gtrsim 5$, $\sigma \gtrsim 40$, $\tau \lesssim 25$, $\angle i \gtrsim 40$, $Y \lesssim 50$, and $A_v^{los} \sim$ 100–300. These values translate into typical torus sizes and masses of 0.1–5.0 pc and 10^4–$10^6 M_{\odot}$.
4. About half of the objects require an additional blackbody component in the near-IR range to provide an adequate fit to the SEDs. Most of best-fitted temperatures are very high ($T \sim$ 1700–2500 K) and cannot correspond to the emission of hot dust.
5. 2pC models can sometimes provide a better fit to sources that require additional near-IR flux.
6. We find weak evidence that nuclei with HBLRs present lower levels of extinction than those without an HBLR.
7. Tentatively, we find that radio-loud objects are those with a very small inclination angle with respect to the line of sight.
8. We find no correlation between the torus properties and the presence of star formation.

and Robert Nikutta from the Department of Astronomy at the Kentucky University, home of the Clumpy code and models, for all their help and guidance. Finally, we are grateful to Patrick Roche and Emeric Le Floc'h for sharing their spectroscopic observations with us.

REFERENCES

Alexander, D. M. 2001, MNRAS, 320, L15
Alonso-Herrero, A., Quillen, A. C., Rieke, G. H., Ivanov, V. D., & Efstathiou, A. 2003, AJ, 126, 81
Alonso-Herrero, A., Ramos Almeida, C., Mason, R., et al. 2011, ApJ, 736, 82 (AH11)
Antonucci, R. 1993, ARA&A, 31, 473
Asensio Ramos, A., & Ramos Almeida, C. 2009, ApJ, 696, 2075
Barger, A. J., Cowie, L. L., Mushotzky, R. F., et al. 2005, AJ, 129, 578
Bassani, L., Dadina, M., Maiolino, R., et al. 1999, ApJS, 121, 473
Bassani, L., Molina, M., Malizia, A., et al. 2006, ApJL, 636, L65
Beckert, T., Driebe, T., Hönig, S. F., & Weigelt, G. 2008, A&A, 486, L17
Bonning, E. W., Bailyn, C., Urry, C. M., et al. 2009, ApJL, 697, L81
Brightman, M., & Nandra, K. 2008, MNRAS, 390, 1241
Buchanan, C. L., Kastner, J. H., Forrest, W. J., et al. 2006, AJ, 132, 1890
Chiaberge, M., Capetti, A., & Celotti, A. 1999, A&A, 349, 77
Côté, P., Piatek, S., Ferrarese, L., et al. 2006, ApJS, 165, 57
Deluit, S. J. 2004, A&A, 415, 39
Deo, R. P., Crenshaw, D. M., Kraemer, S. B., et al. 2007, ApJ, 671, 124
Deo, R. P., Richards, G. T., Nikutta, R., et al. 2011, ApJ, 729, 108
Díaz-Santos, T., Charmandaris, V., Armus, L., et al. 2010, ApJ, 723, 993
Efstathiou, A., & Rowan-Robinson, M. 1995, MNRAS, 273, 649
Elitzur, M. 2012, ApJL, 747, L33
Elvis, M., Risaliti, G., Nicastro, F., et al. 2004, ApJL, 615, L25
Falcke, H., Körding, E., & Markoff, S. 2004, A&A, 414, 895
Fritz, J., Franceschini, A., & Hatziminaoglou, E. 2006, MNRAS, 366, 767
Gallimore, J. F., Axon, D. J., O'Dea, C. P., Baum, S. A., & Pedlar, A. 2006, AJ, 132, 546
Gaskell, C. M., Goosmann, R. W., Antonucci, R. R. J., & Whysong, D. H. 2004, ApJ, 616, 147
Gilli, R., Comastri, A., & Hasinger, G. 2007, A&A, 463, 79
Granato, G. L., & Danese, L. 1994, MNRAS, 268, 235
Greenhill, L. J., Tilak, A., & Madejski, G. 2008, ApJL, 686, L13
Gregory, P. C., Vavasour, J. D., Scott, W. K., & Condon, J. J. 1994, ApJS, 90, 173
Gu, Q., Maiolino, R., & Dultzin-Hacyan, D. 2001, A&A, 366, 765
Haas, M., Siebenmorgen, R., Pantin, E., et al. 2007, A&A, 473, 369
Heisler, C. A., Lumsden, S. L., & Bailey, J. A. 1997, Natur, 385, 700
Hewitt, A., & Burbidge, G. 1991, ApJS, 75, 297
Ho, L. C. 1999, ApJ, 516, 672
Hönig, S. F., Beckert, T., Ohnaka, K., & Weigelt, G. 2006, A&A, 452, 459
Hopkins, P. F., Richards, G. T., & Hernquist, L. 2007, ApJ, 654, 731
Ivezić, Z., Nenkova, M., & Elitzur, M. 1999, arXiv:astro-ph/9910475
Jaffe, W., Meisenheimer, K., Röttgering, H., Leinert, C., & Richichi, A. 2004, in IAU Symp. 222, The Interplay Among Black Holes, Stars and ISM in Galactic Nuclei, ed. T. Storchi-Bergmann, L. C. Ho, & H. R. Schmitt (Cambridge: Cambridge Univ. Press), 37
Kellermann, K. I., Sramek, R., Schmidt, M., Shaffer, D. B., & Green, R. 1989, AJ, 98, 1195
Kishimoto, M., Hönig, S. F., Antonucci, R., et al. 2009a, A&A, 507, L57
Kishimoto, M., Hönig, S. F., Antonucci, R., et al. 2011, A&A, 536, A78
Kishimoto, M., Hönig, S. F., Tristram, K. R. W., & Weigelt, G. 2009b, A&A, 493, L57
LaMassa, S. M., Heckman, T. M., Ptak, A., et al. 2010, ApJ, 720, 786
Lamastra, A., Bianchi, S., Matt, G., et al. 2009, A&A, 504, 73
Landt, H., Elvis, M., Ward, M. J., et al. 2011, MNRAS, 414, 218
Lawrence, A., & Elvis, M. 1982, ApJ, 256, 410
Le Floc'h, E., Mirabel, I. F., Laurent, O., et al. 2001, A&A, 367, 487
Levenson, N. A., Sirocky, M. M., Hao, L., et al. 2007, ApJL, 654, L45
Lumsden, S. L., & Alexander, D. M. 2001, MNRAS, 328, L32
Lumsden, S. L., Alexander, D. M., & Hough, J. H. 2004, MNRAS, 348, 1451
Maccacaro, T., Perola, G. C., & Elvis, M. 1982, ApJ, 257, 47
Maiolino, R., Marconi, A., & Oliva, E. 2001a, A&A, 365, 37
Maiolino, R., Marconi, A., Salvati, M., et al. 2001b, A&A, 365, 28
Maiolino, R., Salvati, M., Bassani, L., et al. 1998, A&A, 338, 781
Malkan, M. A., Gorjian, V., & Tam, R. 1998, ApJS, 117, 25
Marconi, A., Risaliti, G., Gilli, R., et al. 2004, MNRAS, 351, 169
Mason, R. E., Wright, G., Pendleton, Y., & Adamson, A. 2004, ApJ, 613, 770
Mass-Hesse, J. M., Rodriguez-Pascual, P. M., Mirabel, I. F., & Sanz Fernandez de Cordoba, L. 1993, in Proc. 8th IAP Astrophysics Meeting, First Light in the Universe. Stars or QSO's?, ed. B. Rocca-Volmerange, B. Guiderdoni, M. Dennefeld & J. Tran Thanh Van (Gif-sur-Yvette: Editions Frontiers), 397
Mathis, J. S., Rumpl, W., & Nordsieck, K. H. 1977, ApJ, 217, 425
Meisenheimer, K., Tristram, K. R. W., Jaffe, W., et al. 2007, A&A, 471, 453
Meléndez, M., Kraemer, S. B., Armentrout, B. K., et al. 2008, ApJ, 682, 94
Mor, R., Netzer, H., & Elitzur, M. 2009, ApJ, 705, 298
Mor, R., & Trakhtenbrot, B. 2011, ApJL, 737, L36
Mullaney, J. R., Alexander, D. M., Goulding, A. D., & Hickox, R. C. 2011, MNRAS, 414, 1082
Nenkova, M., Ivezić, Ž., & Elitzur, M. 2002, ApJL, 570, L9
Nenkova, M., Sirocky, M. M., Ivezić, Ž., & Elitzur, M. 2008a, ApJ, 685, 147
Nenkova, M., Sirocky, M. M., Nikutta, R., Ivezić, Ž., & Elitzur, M. 2008b, ApJ, 685, 160
Nenkova, M., Sirocky, M. M., Nikutta, R., Ivezić, Ž., & Elitzur, M. 2010, ApJ, 723, 1827
Nikutta, R., Elitzur, M., & Lacy, M. 2009, ApJ, 707, 1550
Noguchi, K., Terashima, Y., Ishino, Y., et al. 2010, ApJ, 711, 144
Panessa, F., & Bassani, L. 2002, A&A, 394, 435
Pier, E. A., & Krolik, J. H. 1992, ApJ, 401, 99
Pier, E. A., & Krolik, J. H. 1993, ApJ, 418, 673
Raban, D., Jaffe, W., Röttgering, H., Meisenheimer, K., & Tristram, K. R. W. 2009, MNRAS, 394, 1325
Ramos Almeida, C., Levenson, N. A., Rodríguez Espinosa, J. M., et al. 2009, ApJ, 702, 1127 (RA09)
Reichert, G. A., Mushotzky, R. F., Holt, S. S., & Petre, R. 1985, ApJ, 296, 69
Risaliti, G., Elvis, M., Fabbiano, G., Baldi, A., & Zezas, A. 2005, ApJL, 623, L93
Risaliti, G., Maiolino, R., & Salvati, M. 1999, ApJ, 522, 157
Roche, P. F., Packham, C., Aitken, D. K., & Mason, R. E. 2007, MNRAS, 375, 99
Rush, B., Malkan, M. A., & Spinoglio, L. 1993, ApJS, 89, 1
Sazonov, S., Revnivtsev, M., Krivonos, R., Churazov, E., & Sunyaev, R. 2007, A&A, 462, 57
Schartmann, M., Meisenheimer, K., Camenzind, M., Wolf, S., & Henning, T. 2005, A&A, 437, 861
Shakura, N. I., & Sunyaev, R. A. 1976, MNRAS, 175, 613
Shi, Y., Rieke, G. H., Hines, D. C., et al. 2006, ApJ, 653, 127
Shu, X. W., Wang, J. X., Jiang, P., Fan, L. L., & Wang, T. G. 2007, ApJ, 657, 167
Siebenmorgen, R., Haas, M., Krügel, E., & Schulz, B. 2005, A&A, 436, L5
Smith, D. A., & Done, C. 1996, MNRAS, 280, 355
Smith, J. D. T., Draine, B. T., Dale, D. A., et al. 2007, ApJ, 656, 770
Stalevski, M., Fritz, J., Baes, M., Nakos, T., & Popović, L. Č. 2012, MNRAS, 420, 2756
Suganuma, M., Yoshii, Y., Kobayashi, Y., et al. 2006, ApJ, 639, 46
Swain, M., Vasisht, G., Akeson, R., et al. 2003, ApJL, 596, L163
Taranova, O. G., & Shenavrin, V. I. 2006, AstL, 32, 439
Thean, A., Pedlar, A., Kukula, M. J., Baum, S. A., & O'Dea, C. P. 2000, MNRAS, 314, 573
Thompson, G. D., Levenson, N. A., Uddin, S. A., & Sirocky, M. M. 2009, ApJ, 697, 182
Tommasin, S., Spinoglio, L., Malkan, M. A., & Fazio, G. 2010, ApJ, 709, 1257
Tran, H. D. 2001, ApJL, 554, L19
Tran, H. D. 2003, ApJ, 583, 632
Tristram, K. R. W., Meisenheimer, K., Jaffe, W., et al. 2007, A&A, 474, 837
Tristram, K. R. W., Raban, D., Meisenheimer, K., et al. 2009, A&A, 502, 67

Turner, T. J., George, I. M., Nandra, K., & Mushotzky, R. F. 1997, ApJS, 113, 23

Veron-Cetty, M.-P., & Veron, P. 1991, ESOSR, 10, 1

Videla, L., Lira, P., Andrews, H., et al. 2013, ApJS, 204, 23 (Paper I)

Walcher, C. J., Böker, T., Charlot, S., et al. 2006, ApJ, 649, 692

Weigelt, G., Wittkowski, M., Balega, Y. Y., et al. 2004, A&A, 425, 77

Weinberger, A. J., Neugebauer, G., & Matthews, K. 1999, AJ, 117, 2748

Winter, L. M., Mushotzky, R. F., Tueller, J., & Markwardt, C. 2008, ApJ, 674, 686

Wittkowski, M., Balega, Y., Beckert, T., et al. 1998, A&A, 329, L45

Wittkowski, M., Kervella, P., Arsenault, R., et al. 2004, A&A, 418, L39

Wu, Y., Charmandaris, V., Huang, J., Spinoglio, L., & Tommasin, S. 2009, ApJ, 701, 658

Zhang, E.-P., & Wang, J.-M. 2006, ApJ, 653, 137